Unifying bilateral teleoperation and tele-impedance for enhanced user experience

Marco Laghi[1,3], Arash Ajoudani[2], Manuel G. Catalano[1], and Antonio Bicchi[1,3]

Abstract

Usability is one of the most important aspects of teleoperation. Ideally, the operator's experience should be one of complete *command* over the remote environment, but also be as close as possible to what s/he would have if physically present at the remote end - i.e. *transparency* in terms of both action and perception. These two aspects may coincide in favorable conditions, where classic approaches such as the four-channel architecture ensures transparency of the control framework. In presence of substantial delays between the user and the slave, however, the stability-performance trade-off inherent to bilateral teleoperation deteriorates not only transparency, but also command. An alternative, unilateral approach is given by tele-impedance, which controls the slave-environment interaction by measuring and remotely replicating the user's limb endpoint position and impedance. Not including force feedback to the operator, tele-impedance is absolutely robust to delays, while it completely lacks transparency.

This paper introduces a novel control framework which integrates a new, fully transparent, two-channel bilateral architecture with the tele-impedance paradigm. The result is a unified solution that mitigates problems of classical approaches, and provides the user with additional tools to modulate the slave robot's physical interaction behavior, resulting in a better operator experience in spite of time inconsistencies. The validity and effectiveness of the proposed solution is demonstrated in terms of performance in the interaction tasks, of user fatigue and overall experience.

1 Introduction

In the last years, the social interest in remotely-operated robots has been sharpened because of the possibility of use in situations dangerous for men, to substitute the risky presence of humans with robot avatars. Examples are space (Imaida et al. 2004; Wright et al. 2005; Artigas et al. 2016) and underwater (Khatib et al. 2016) applications, dangerous (Desbats et al. 2006; Pratt and Manzo 2013), rescue/inspection (Negrello et al. 2018) and industry (Shukla and Karki 2016) scenarios. A big incentive came from the DARPA Robotics Challenge (DRC) (Pratt and Manzo 2013), which tested the ability of several humanoids to face and accomplish different tasks typically needed after natural or man-made disasters, as e.g. removing debris blocking an entryway, using a cutting tool, and turning a valve near a leaking pipe. Even if the DRC pushed forward the boundaries on autonomous operation of such platforms, the majority of the results were achieved through direct teleoperation actions (Guizzo and Ackerman 2015; Schwarz et al. 2017). This is because the problem-solving ability and versatility, typical of humans, needed in those kind of situations are far from been achieved by the current levels of robot intelligence. As a consequence, the aim of direct teleoperation applications, in which the user has full and direct control of the robot movements, is to exploit these human skills and, therefore, compensate for the lack of current robot autonomy levels.

To enable robot operators to "see, feel, and control" direct interactions on remote environments using robotic systems, the requirements are: 1- to build a system that is able to transfer the user's movements and intentions to the robotic counterpart, and 2- to make the user perfectly perceive the remote environment. The first requirement concerns the tracking of the user's positions/velocities as references to the slave, as well as the forces generated through dynamical interaction with the environment. This set of information enables the slave to achieve a human-like physical interaction performance. The perception requirement is because the high ability of humans to physically act in, interact with and adapt to the surroundings is due, first of all, to their capacity to perceive and interpret the environment through two main senses: vision and touch. Then, in a direct teleoperation, vision and force feedbacks are both extremely important and if fully and correctly provided to the user, can make him/her perfectly perceive the remote environment and experience a satisfactory sense of *telepresence* (Held and Durlach 1992; Niemeyer et al. 2008). Finally, the two requirements above

[0][1]Soft Robotics for Human Cooperation and Rehabilitation (SoftBots), Istituto Italiano di Tecnologia, Genoa, IT.
[2]Human-Robot Interfaces and Physical Interaction (HRI[2]), Istituto Italiano di Tecnologia, Genoa, IT.
[3]Centro di Ricerca "E. Piaggio", Universita di Pisa, Pisa, IT.
[0]

Corresponding author:
Marco Laghi
Soft Robotics for Human Cooperation and Rehabilitation (SoftBots)
Istituto Italiano di Tecnologia
Via Morego, 30, 16163, Genova, Italy
[0]Email: marco.laghi@iit.it

are essential to obtain an high level of usability of the framework and enable a valid user's experience.

From the control point of view, perfect telepresence of a general teleoperation system (depicted in Fig. 1) is a synonyms of *full transparency* (Raju et al. 1989), commonly achieved through the classic four-channel architecture (Lawrence 1993) (Fig. 2(a)). In this scheme the master and the slave are strongly coupled, since both depend on the position of the other, as well as on the sensed forces. As a consequence, the existence of delays in the communication channels produces three main undesired effects, which eventually undermine the framework's usability:

1. System stability is not automatically ensured, since the delays are included in the control loop between the master and slave sides (see Fig. 2(a));
2. a 'phantom force' which is perceived by the human operation but does not correspond to any remote interaction (see Sec. 3 for details);
3. the transparency performance is deteriorated, since the user's action is delayed as well as the forces and images fed back to him/her, resulting in a distorted perception of the remote interactions.

These three issues will be well reasoned in Section 2.

A partial solution to this problem can be represented by the concept of tele-impedance control (Ajoudani et al. 2012), introduced by our group few years ago, a unilateral approach with which the user's intention is transferred to the robotic counterpart, enabling a sort of continue remote presence, despite any delay. Nonetheless, the force feedback would remain the first choice when a high degree of transparency is required to accomplish complex remote manipulation tasks.

Addressing all the issues above, this paper aims to find a solution that mitigates the problems of classical teleoperation approaches and enhances their usability. The result is a framework that, even by using a reduced number of communications channels, respects full transparency, an essential requirement for high quality applications. This simplifies the design of the passivity layer (due to the reduced number of communicated signals, e.g. compared to the four-channel architecture (Artigas et al. 2016; Rebelo and Schiele 2015)) and augments its robustness with respect to delays (as in Laghi et al. (2017)). In the proposed framework, the tele-impedance paradigm is integrated to

subsume its characteristics and improve the user's remote presence and the slave robot's adaptation capacity to the external disturbances and task requirements, especially in the presence of communication delays. Moreover, the resulting unified bilateral teleoperation architecture eliminates the 'phantom force'. This, together with the new tools provided by tele-impedance, strongly increases the usability of the system, as well as the user's experience quality, as it will be demonstrated with the results of this work.

Two different multi degrees-of-freedom hardware setups that will enable the execution of complex realistic manipulation tasks in environments with dynamic uncertainties are introduced, and then used to perform multi-subject experiments, specifically designed to evaluate the performances during complex dynamic interaction with several communication delay profiles. Extensive results are reported, in order to properly assert the usability and advantages of the proposed architecture. The performances are then evaluated on an objective and subjective levels: the first one involves the analysis of the interacting forces with the remote environment, as well as physiological signals correlated with the subjects fatigue; the second one is carried through questionnaires that try to assess the subjects experience and preferences.

A qualitative comparison between classic four-channel framework (4C), the new proposed two-channel fully transparent framework (FT^2) and the one augmented with tele-impedance ($TIFT^2$) is reported in Table 1 and will be quantitatively demonstrated by the experimental results of this work. As summarized in the table, $TIFT^2$ inherits the advantages of full transparency (as perception and reaction) from 4C and the robustness and adaptability to environmental interactions in presence of delays from tele-impedance.

The rest of this paper is structured as follows: Section 2 explain the issues given by communication delays introduced before, and reports a summarized overview of the solutions offered in the literature that deal with transparency and stability in bilateral teleoperation. In Section 3 a deep analysis on how the choice of local master-slave controllers can modify the structure of a classic four-channel architecture while maintaining full transparency shows the path to reach the final two-channel architecture. The application of one of the stability controls introduced in Section 2, i.e. the Time Domain Passivity Approach (TDPA), to the final framework follows in Section 4, together with the implementation of a new solution that avoid position drift in position-based controls. Section 5 recalls the tele-impedance paradigm and shows its integration in the new, fully transparent, two-channel bilateral architecture. Section 6 presents the experimental setup as well as the results of the multi-subject experiments, while a discussion of the achievements is provided in Section 7. Finally, conclusions are synthesized in Section 8.

Table 1. Characteristics of classic four-channel architectures (4C), the new proposed two-channel fully transparent framework (FT^2) and the one integrating the tele-impedance paradigm ($TIFT^2$).

	4C	**FT^2**	**$TIFT^2$**
NUMBER OF TRANSMITTED SIGNALS	4	2	3
TRANSPARENCY (W/O DELAY)	✓	✓	✓
STABILITY ROBUSTNESS W.R.T. DELAYS	✓*	✓*	✓*
'PHANTOM FORCE' EFFECT (W/ DELAY)	✓	✗	✗
INTERACTION ADAPTABILITY W/ DELAY	LOW	LOW	HIGH
USER FATIGUE WITH DELAY W/ DELAY	HIGH	LOW	LOW
DAMAGE RISKS DURING UNFORESEEN INTERACTIONS (ESPECIALLY W/ DELAY)	HIGH	HIGH	LOW

*All of them work well with communication delays only under the presence of a passivity controller. However, since master and slave are less coupled, FT^2 and $TIFT^2$ need less passivisation action (similarly to the TIFF architecture presented in Laghi et al. (2017))

2 About transparency, stability and usability in bilateral teleoperation

As anticipated in the Introduction, from a control point of view perfect telepresence is equivalent to full transparency (Raju et al. 1989). Transparency is a well-known and

extensively studied research topic, with works proposing solutions for transparency-optimized control architectures, such as in Hannaford (1989); Salcudean et al. (2000); Hashtrudi-Zaad (2000); Hirche et al. (2005); Alfi and Farrokhi (2008). A thorough review of the progress achieved through the years is presented in Hokayem and Spong (2006). Generally, the conditions to achieve full transparency are implemented through the classic four-channel architecture (Lawrence 1993) (Fig. 2(a)), later also expanded in Hashtrudi-Zaad and Salcudean (2001). Based on this last, in Hashtrudi-Zaad and Salcudean (2002) two three-channel solutions (*Operator-Force-Compensated (OFC)* and *Environment-Force-Compensated (EFC)*) that respect full transparency requirements are presented.

As suggested in the Introduction, beside transparency, the system stability is a mandatory requirement for teleoperation systems, threatened by the presence of delays in the information exchange between the local (master) and remote (slave) sides. Indeed, communication delays have generally the three main undesired effects listed in the Introduction: 1- system stability blackmail; 2- phantom force generation; 3 - transparency performance deterioration.

The stability issues have been successfully solved in the last decades through various approaches, most of them using the conservative concept of passivity. The most classic of these solutions are delay-dependent (Anderson and Spong 1989; Niemeyer and Slotine 1997), or model-dependent (Natori et al. 2010; Suzuki and Ohnishi 2013; Smith 1959). More recently, two new techniques, both model and delay independent, have been proposed. The first one is the Time Domain Passivity Approach (TDPA) that ensures the passivity of the communication channel. It was firstly presented for the position-force teleoperation architecture (Hannaford and Ryu 2002) and then adapted to a position-position (Artigas et al. 2010) and four-channel frameworks (Artigas et al. 2016; Rebelo and Schiele 2015). An extension of this work has been also used in Balachandran et al. (2017) for explicit force control. The second one is the Energy Tank approach (Franken et al. 2011) that, differently from TDPA, takes into account the whole system passivity. It has been also applied to haptics scenario (Pacchierotti et al. 2015), tele-surgery (Ferraguti et al. 2015), and remote needle insertion and palpation (Meli et al. 2017). All these techniques damp/cut some variables of the control loops, basically modifying the desired action demanded by the transparent architecture (i.e., the user's feedback and the remote robot action) and then contributing to deteriorate the telepresence. For example, in Laghi et al. (2017) it has been shown that in the classic four-channel the strong master-slave coupling causes an high sensibility of the framework with respect to communication delays that provokes a strong intervention of the passivity controllers and, consequently, the alteration of the original desired control. Find a solution that shows a better robustness to delays can then be beneficial for the general performances of the application and its usability.

As it will be explained in the following (Section 3) and shown in the experimental section, the 'phantom force' phenomenon affects the user's perception and comfort with direct consequences, again, on the usability and performances of the teleoperation framework. This effect has been previously described as 'operational force' by Iida and Ohnishi (2004), and 'coordinating force' by e.g. Hashtrudi-Zaad and Salcudean (2001). To avoid confusion, we will refer to the more intuitive phantom force term. In this work, we will provide the total cancellation of the phenomenon through a smart choice of the architecture controllers and avoiding the addition of other components as force observers.

Lastly, the deterioration of transparency is also simply caused by the temporal discrepancies between the action and perception at both local and remote sides and it is unavoidable, as long as delays in the communication occur.

Tele-impedance (Ajoudani et al. 2012) could be an approach able to partially mitigate these temporal discrepancies. Tele-impedance consists of measuring the master's limb impedance along with the position trajectories, and feeding them forward in real-time to the slave as references, which are then replicated by local controllers (Ajoudani 2016). This approach was conceived to address the problem of unconditional stability and contact efficiency while interacting with unstructured environments and so it doesn't include any force feedback to the user and, consequently, does not require a master haptic interface. While low impedance values commanded by the master's limb would enhance the robot's adaptivity to the environmental constraints, stiffer profiles can generate more accurate interaction between the slave robot and the environment. In addition, the feed-forward nature of the control scheme makes it robust against the low-quality communication channels. Despite this, the force feedback would remain the first choice when a high degree of transparency is required to accomplish complex remote manipulation tasks.

A completely different but noteworthy approach for bilateral teleoperation offered in the literature is the *model-mediated* teleoperation (MMT) (Mitra and Niemeyer 2008). In MMT, the forces/velocities sensed at the remote side are not directly fed back to the operator. Instead, s/he interact with a local model of the remote environment, constantly updated based on the information received. MMT applications face as well the problems of transparency and stability.

Transparency performances are strictly correlated to the technique used for the environment modeling. It can be performed using any information received from the remote side. A good example is the sensory-fusion approach implemented in Xu et al. (2014). An overview of existing techniques is available in Xu et al. (2016).

On the other side, the model update is a possible cause of instability. This update, practically, changes the impedance displayed to the user. If suddenly and/or not properly updated, a jump in the force rendered to the operator can occur. Citing Xu et al. (2016): "*if the users cannot adjust their arm impedance quickly enough to follow (stabilize) this force change, an unexpected motion occurs, causing dangerous slave behavior*" and, in the worth cases, leading to instability. The solutions available for MMT stability control are smooth and stable environment model update techniques, as *zero* and *non-zero energy injections* (see Xu et al. (2016)). As for the direct bilateral teleoperation stability controls mentioned above, also the methods used to stabilize MMT framework are based on passivity conditions.

MMT is a really promising and relatively new approach to bilateral teleoperation. It implicitly solve the problem of the phantom force, since the operator interacts with a local model and no delay is present between him/her and the model s/he interacts with. Nonetheless, stability problems are still present, as just explained. Moreover, the performances of the model estimation techniques are far from achieving full transparency condition (1), compared to the solutions offered by direct teleoperation listed above.

This work tries to mitigate the classical problems of direct bilateral teleoperation discussed above. With this aim, the solutions introduced can be summarized in the three following points:

1. The definition of a new two channel fully transparent architecture, called FT^2, that reduces the number of communicated signals to two and eliminates the phantom force problem. Therefore, it relaxes the coupling between master and slave and requires less effort from the operator, particularly beneficial in presence of high communication delays.

2. The inclusion of the tele-impedance paradigm in the FT^2, with the consequent definition of the fully transparent TIFT^2 architecture. Including the benefits introduced by FT^2, this solution also provides the user with an additional control degree of the slave counterpart, i.e. its impedance profile. It helps in the compensation of the temporal impedance mismatch between user and slave in presence of high delays, and enables a better regulation of the remote interaction forces. A first attempt to provide a solution similar to the above was proposed in Laghi et al. (2017). However, the present work is fundamentally different since it focuses on the usability assessment of the different architectures in terms of user experience and preferences in various conditions. This is reflected in the assurance of full transparency, which is not granted in Laghi et al. (2017)), and the thorough experimental validation on a complete 6 DOF system.

3. A particular implementation of the TDPC for position-based control, expanding on the idea preliminarily presented in Laghi et al. (2017) among others, which avoids position drift and also permits to passivate the impedance controller. This latter aspect is fundamental to the TIFT^2, as it allows to implicitly ensure the stability of the framework despite on-line changes of the slave impedance profile.

3 Full transparency in teleoperation systems

The most general teleoperation system is represented by the two-port model depicted in Fig. 1, where Z_h and Z_e, V_h and V_e, and F_h and F_e are the impedances, velocities and forces of the local operator (human) and remote environment, respectively, while Z_t is the impedance rendered to the operator by the teleoperator interface T. This last includes master interface and slave interface, as well as all the controllers and the communication channel. The term *transparency* refers to the possibility to have a teleoperator interface that result transparent with respect the physical link between the operator and the remote environment. It follows that full transparency is achieved when the impedance Z_t transmitted by the teleoperation system to the human is the
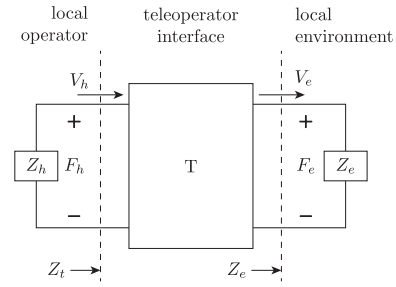
Figure 1. General two-port model of a bilateral teleoperation system (from Lawrence (1993)).

same as the one of the remote environment Z_e:

$$Z_t = Z_e. \tag{1}$$

The relation between the variables of the two-port model of Fig. 1 can be formulated in several ways (see e.g Aliaga, Rubio and Sanchez (2004)). Most common is probably the hybrid matrix formulation (Hannaford 1989; Lawrence 1993):

$$\begin{bmatrix} F_h \\ V_h \end{bmatrix} = H \begin{bmatrix} V_e \\ -F_e \end{bmatrix} = \begin{bmatrix} H_{11} & H_{12} \\ H_{21} & H_{22} \end{bmatrix} \begin{bmatrix} V_e \\ -F_e \end{bmatrix}, \tag{2}$$

from which

$$F_h = \underbrace{\frac{H_{11} - H_{12}Z_e}{H_{21} - H_{22}Z_e}}_{=Z_t} V_h, \tag{3}$$

with Z_t being the transmitted impedance. The general solution for the hybrid matrix that allows (1) is

$$H_{11} = 0; H_{12} = -I; H_{21} = I; H_{22} = 0.$$
$$\Downarrow \tag{4}$$
$$H = \begin{bmatrix} 0 & -I \\ I & 0 \end{bmatrix},$$

that means $F_h = F_e$ and $V_e = V_h$. In case of communication delays between the local and remote sides, the ideal *delayed impedance matching* (Hashtrudi-Zaad and Salcudean 2002) is verified when $V_e = e^{-sT_1}V_h$ and $F_h = e^{-sT_2}F_e$:

$$H_{11} = 0; H_{12} = -e^{-sT_2}; H_{21} = e^{sT_1}; H_{22} = 0.$$
$$\Downarrow \tag{5}$$
$$H = \begin{bmatrix} 0 & -e^{-sT_2} \\ e^{sT_1} & 0 \end{bmatrix},$$

with T_1 and T_2 being the forward (master-to-slave) and backward (slave-to-master) delays, respectively. In this case, the transmitted impedance Z_t of (3) is

$$Z_t = \frac{H_{11} - H_{12}Z_e}{H_{21} - H_{22}Z_e} = \frac{e^{-sT_2}}{e^{sT_1}}Z_e = e^{-sT_{rt}}Z_e, \tag{6}$$

where $T_{rt} = T_1 + T_2$ is the round-trip delay. It means that, with delayed communication, the ideal transmitted impedance Z_t is equal to Z_e delayed by the round-trip delay T_{rt}. If the two delays are null ($T_1 = T_2 = 0$), (5) is equivalent to (4), and so (6) to (1).

It is well known, and stated in Lawrence (1993), that a sufficient condition to achieve full transparency in absence of

communication delays is through four-channel architecture (4C). The four-channel scheme is shown in Fig. 2(a), where subscripts h, m, s and e stand for human, master, slave and environment, and Z_h, Z_m, Z_s and Z_e are the relative impedances in operational space. C_m and C_s are the local controllers, while $C_i, i = 1, \ldots, 4$ are the controllers of the forces/velocities transmission. e^{-sT_1} is the channel delay of T_1 seconds from master to slave and e^{-sT_2} is the channel delay of T_2 seconds from slave to master. $V_m(s) \equiv V_h(s)$ and $V_s(s) \equiv V_e(s)$ are the velocity of the master, human, slave and environment. $F_h(s) = F_h^*(s) + Z_h(s)V_h(s)$ is the sum of the force produced by "voluntary" action of the user $F_h^*(s)$ and the one produced by its impedance $Z_h(s)V_h(s)$. Hypothesizing an active environment, the same can be explained for $F_e(s) = F_e^*(s) + Z_e(s)V_e(s)$. For sake of clarity and compactness, the dependence of the various variables/functions from s will be omitted where not necessary in the following. Furthermore, in the whole paper a variable written with capital letter is expressed in the Laplace domain, while with a small letter is referred to the time domain (e.g. master velocity: V_m and v_m), if not differently indicated. The resulting forces applied to the master and slave robot structures $F_{m,tot}$ and $F_{s,tot}$ are

$$
\begin{aligned}
F_{m,tot} &= F_h \overbrace{-C_m V_m - C_2 e^{-sT_2} F_e - C_4 e^{-sT_2} V_s}^{F_{C_m,tot}}; \\
F_{s,tot} &= -F_e \underbrace{-C_s V_s + C_3 e^{-sT_1} F_h + C_1 e^{-sT_1} V_m}_{F_{C_s,tot}},
\end{aligned}
\tag{7}
$$

where $F_{C_m,tot}$ and $F_{C_s,tot}$ are the total forces commanded by the various controllers to the master and the slave, respectively. Considering that $F_{m,tot}$ and $F_{s,tot}$ are the total forces applied to master and slave, respectively, and therefore the dynamic relations $Z_m V_m = F_{C_m,tot}$ and $Z_s V_s = F_{C_s,tot}$ hold, the elements H_{ij} with $i, j = 1, 2$ of the hybrid matrix H in (2) for the 4C architecture of Fig. 2(a) are

$$
\begin{aligned}
H_{11} &= \frac{(Z_m + C_m)(Z_s + C_s - e^{-sT_{rt}} C_3 C_4)}{e^{-sT_1}(C_1 + C_3 Z_m + C_3 C_m)} + e^{-sT_2} C_4; \\
H_{12} &= -\frac{(Z_m + C_m)(I - e^{-sT_{rt}} C_3 C_2)}{e^{-sT_1}(C_1 + C_3 Z_m + C_3 C_m)} - e^{-sT_2} C_2; \\
H_{21} &= \frac{Z_s + C_s - e^{-sT_{rt}} C_3 C_4}{e^{-sT_1}(C_1 + C_3 Z_m + C_3 C_m)}; \\
H_{22} &= \frac{I - e^{-sT_{rt}} C_3 C_2}{e^{-sT_1}(C_1 + C_3 Z_m + C_3 C_m)}.
\end{aligned}
\tag{8}
$$

In Lawrence (1993) it is stated that, in the absence of delays, complete transparency (4) is achieved if and only if

$$
\begin{aligned}
C_2 C_3 &= I; \\
C_1 &= (Z_s + C_s); \\
C_4 &= -(Z_m + C_m).
\end{aligned}
\tag{9}
$$

As long as $C_i, i = [1, 4]$ are designed to respect the conditions of (9) and no delay is present, the transparency is always achieved, independently from the choice of C_s and C_m. In general, the first equation of (9) is solved setting $C_2 = C_3 = I$.

The elements (8) of the hybrid matrix in this case become

$$
C_1 = (Z_s + C_s); C_2 = I; C_3 = I; C_4 = -(Z_m + C_m).
$$

$$
\Downarrow \text{ in } (8)
$$

$$
\begin{aligned}
H_{11} &= \frac{(Z_m + C_m)\left[Z_s + C_s + e^{-sT_{rt}}(Z_m + C_m)\right]}{e^{-sT_1}(Z_m + C_m + Z_s + C_s)} - e^{-sT_2}(Z_m + C_m); \\
H_{12} &= -\frac{(Z_m + C_m)(I - e^{-sT_{rt}})}{e^{-sT_1}(Z_m + C_m + Z_s + C_s)} - e^{-sT_2}; \\
H_{21} &= \frac{Z_s + C_s + e^{-sT_{rt}}(Z_m + C_m)}{e^{-sT_1}(Z_m + C_m + Z_s + C_s)}; \\
H_{22} &= \frac{I - e^{-sT_{rt}}}{e^{-sT_1}(Z_m + C_m + Z_s + C_s)}.
\end{aligned}
\tag{10}
$$

It is easy to check that, setting $T_1 = T_2 = 0$ the conditions of (4) are verified.

From (9), it is possible to see that two "control variables" are available: C_m and C_s. In classic applications, as in Lawrence (1993), these two are set as $C_* = Z_{C_*}$ with $* = m, s$ and $Z_{C_*} = B_* + K_*/s$, that are impedance controllers. Consequently, we have $C_1 = Z_s + B_s + K_s/s$ and $C_4 = -(Z_m + B_m + K_m/s)$. Substituting these new values in $F_{C_m,tot}$ and $F_{C_s,tot}$ of (7) and rearranging the various terms we have

$$
\begin{aligned}
F_{C_m,tot} &= \overbrace{Z_m e^{-sT_2} V_s}^{\text{master dynamic comp.}} + \overbrace{(B_m + K_m/s)\tilde{V}_m}^{\text{impedance control } Z_{C_m}} - e^{-sT_2} F_e; \\
F_{C_s,tot} &= \underbrace{Z_s e^{-sT_1} V_m}_{\text{slave dynamic comp.}} + \underbrace{(B_s + K_s/s)\tilde{V}_s}_{\text{impedance control } Z_{C_s}} + e^{-sT_1} F_h,
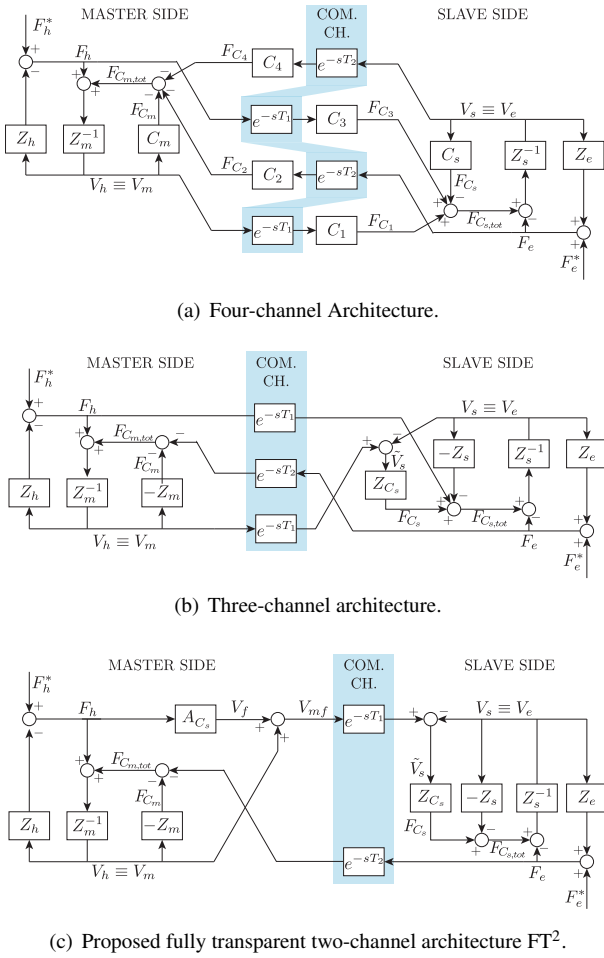\end{aligned}
\tag{11}
$$

where $\tilde{V}_m = (e^{-sT_2} V_s) - V_m$, $\tilde{V}_s = (e^{-sT_1} V_m) - V_s$ are the master and slave velocity tracking errors, respectively. As highlighted in (11), both the total forces include a dynamic compensation depending on the velocity of the other side and an impedance control (Z_{C_m} at the master and Z_{C_s} at the slave) that depends on the relative velocity error.

In this case, the elements of the hybrid matrix H are

$$
C_m = Z_{C_m}; \quad C_s = Z_{C_s}.
$$

$$
\Downarrow \text{ in } (10)
$$

$$
\begin{aligned}
H_{11} &= \frac{(Z_m + Z_{C_m})\left[Z_s + Z_{C_s} + e^{-sT_{rt}}(Z_m + C_m)\right]}{e^{-sT_1}(Z_m + Z_{C_m} + Z_s + Z_{C_s})} - e^{-sT_2}(Z_m + Z_{C_m}); \\
H_{12} &= -\frac{(Z_m + Z_{C_m})(I - e^{-sT_{rt}} I)}{e^{-sT_1}(Z_m + Z_{C_m} + Z_s + Z_{C_s})} - e^{-sT_2}; \\
H_{21} &= \frac{Z_s + Z_{C_s} + e^{-sT_{rt}}(Z_m + Z_{C_m})}{e^{-sT_1}(Z_m + Z_{C_m} + Z_s + Z_{C_s})}; \\
H_{22} &= \frac{I - e^{-sT_{rt}}}{e^{-sT_1}(Z_m + Z_{C_m} + Z_s + Z_{C_s})}.
\end{aligned}
\tag{12}
$$

If no communication delay is present, this solution works perfectly, since it respects transparency requirements of (9). However, when delay is present we see that (12) is far from (6). Moreover, three main problems arise. The major one regards the stability of the system, and will be treated in Sec. 4. The second one regards the dynamic compensation: with the previous choice of C_m and C_s the dynamic compensation of the master/slave robots depends on the velocity of the other side. This means that when a delay is introduced in the system, this compensation is actuated w.r.t. the delayed state of the counterpart, thus contributing to a reduced

(a) Four-channel Architecture.

(b) Three-channel architecture.

(c) Proposed fully transparent two-channel architecture FT².

Figure 2. Block diagram representations of (a) four-channel architecture, (b) three-channel architecture and (c) the proposed fully transparent two-channel architecture FT².

transparency of the system. Lastly, an undesirable force, that we call 'phantom force', is displayed at the side the user is acting, namely the master side. This force is produced by Z_{C_m}: the impedance controller is based on the error $\tilde{V}_m$ between the master velocity V_m and the delayed slave velocity $e^{-sT_2}V_s$. So, when $T_2 \neq 0$, Z_{C_m} displays a force to the user even if the slave is moving in a free environment and no environmental force F_e is sensed (from here the term 'phantom force'). This force is inconsistent with the events at the slave side and could be misinterpreted by the user. The phantom force phenomenon is well-recognizable, for example, in simulation and experimental data reported in (Artigas et al. 2016, 2010; Rebelo and Schiele 2015; Laghi et al. 2017). Notice that the same reasoning can be done also regarding the slave impedance controller.

The problem of dynamic compensation in the presence of delays can be easily solved by choosing to include the dynamic compensation in the associated local controllers C_m and C_s. Indeed, if we choose $C_* = -Z_* + Z_{C_*}$, with $* = m, s$, from (9) we have $C_1 = Z_{C_s} = B_s + K_s/s$ and $C_4 = -Z_{C_m} =$

$-(B_m + K_m/s)$ and, eventually, (11) changes in

$$
F_{C_m,tot} = \overbrace{Z_m V_m}^{\text{m. dynamic comp.}} + \overbrace{(B_m + K_m/s)\tilde{V}_m}^{\text{impedance control } Z_{C_m}} - e^{-sT_2}F_e;
$$
$$
F_{C_s,tot} = \underbrace{Z_s V_s}_{\text{s. dynamic comp.}} + \underbrace{(B_s + K_s/s)\tilde{V}_s}_{\text{impedance control } Z_{C_s}} + e^{-sT_1}F_h, \tag{13}
$$

where the dynamic compensations now depend on the local velocities and aren't affected by the delays. With this choice of C_m and C_s the elements of the hybrid matrix result

$$
C_m = -Z_m + Z_{C_m}; \quad C_s = -Z_s + Z_{C_s}.
$$
$$
\Downarrow \text{ in } (10)
$$
$$
H_{11} = \frac{Z_{C_m}\left(Z_{C_s} + e^{-sT_{rt}}Z_{C_m}\right)}{e^{-sT_1}\left(Z_{C_m} + Z_{C_s}\right)} - e^{-sT_2}Z_{C_m};
$$
$$
H_{12} = -\frac{Z_{C_m}\left(I - e^{-sT_{rt}}\right)}{e^{-sT_1}\left(Z_{C_m} + Z_{C_s}\right)} - e^{-sT_2};
$$
$$
H_{21} = \frac{Z_{C_s} + e^{-sT_{rt}}Z_{C_m}}{e^{-sT_1}\left(Z_{C_m} + Z_{C_s}\right)};
$$
$$
H_{22} = \frac{I - e^{-sT_{rt}}}{e^{-sT_1}\left(Z_{C_m} + Z_{C_s}\right)}. \tag{14}
$$

Regarding the phantom force phenomenon, it could be canceled at both master and slave sides. Under the transparency requirements of (9), this can be achieved by canceling the controllers that handle the velocity communications, C_1 and C_4, then relying only on the communication of the forces F_h and F_e. However, this choice would be problematic, for the following reasons:

a. Dynamic compensation terms are usually subject to uncertainties due to the nonlinearity of the robot dynamics that often is hard to precisely model. This will result in unpredictable position drifts between the master and the slave end-effectors, since no position tracking would foreseen.

b. In presence of any communication delay the stability is always ensured by damping or cutting the command signal (see all the techniques listed in the introduction). So, even assuming a perfect dynamic compensation, damping the forces will again cause a drift between the master and the slave positions.

After these considerations, one possible solution is to eliminate the 'phantom force' at only one side. This means that the side that receives the velocity will follow the other one that, consequently, will lead the motion. A natural choice for these two roles is to elect the master side as leader, while the slave side as follower. This solution is achieved setting $C_2 = C_3 = 1$ and $C_s = -Z_s + Z_{C_s}$, as before, while $C_m = -Z_m$. The resulting channel controllers that allow to respect transparency requirements of (9) are

$$
\begin{aligned}
C_1 &= Z_{C_s} = B_s + K_s/s; \\
C_2 &= 1; \\
C_3 &= 1; \\
C_4 &= 0.
\end{aligned} \tag{15}
$$

and (13) becomes

$$
\begin{aligned}
F_{C_m,tot} &= \overbrace{Z_m V_m}^{\text{m. dynamic comp.}} - e^{-sT_2} F_e; \\
F_{C_s,tot} &= \underbrace{Z_s V_s}_{\text{s. dynamic comp.}} + \underbrace{(B_s + K_s/s)\tilde{V}_s}_{\text{s. impedance controller } Z_{C_s}} + e^{-sT_1} F_h.
\end{aligned}
\tag{16}
$$

The scheme corresponding to (16) is the three-channel framework depicted in Fig. 2(b). In addition to the elimination of the phantom force at the master side and the reduction of the signals transmitted, this solution presents one another advantage: since the control of the position is done only on one side (in this case at the slave side), there's no more the risk of an oscillating behavior due to the virtual spring between master and slave, which is one of the drawbacks of general four-channel or position-position architectures and particularly dangerous in presence of consistent delays, as addressed also in Artigas et al. (2016). The elements of the hybrid matrix (4) resulting from this controllers choice are

$$
C_m = -Z_m; \quad C_s = -Z_s + Z_{C_s}.
$$
$$
\Downarrow \text{ in } (10)
$$
$$
\begin{aligned}
H_{11} &= 0; \\
H_{12} &= -e^{-sT_2}; \\
H_{21} &= e^{sT_1}; \\
H_{22} &= \frac{I - e^{-sT_{rt}}}{e^{-sT_1} Z_{C_s}}.
\end{aligned}
\tag{17}
$$

Compared with the other solutions analyzed above, it is clear that this is the one that get closer to the ideal delayed impedance matching of (6). Moreover, looking at H_{22} in (17) (the only one that differs from the ideal hybrid matrix elements of (5)) it suggests that higher the gains of Z_{C_s} are lower H_{22} is, and closer the ideal impedance matching. High gains could seem a good choice. However, a strong slave impedance controller could be a drawback sometimes, as it will be discussed in Section 5.

This three channel solution is also substantially different from the two proposed in Hashtrudi-Zaad and Salcudean (2002). Indeed, the OFC and EFC, derived from the extended version of the classic four-channel architecture, consist in the communication of both positions/velocities and only one force (F_h for the OFC and F_e for EFC), instead of just one position and both forces. It follows that, in that two cases, the phantom force effect is not avoided.

3.1 Fully Transparent Two-Channel Architecture

Under the condition that the gains of Z_{C_s} are known a priori, it is also possible to avoid the transmission of F_h. Indeed, knowing the parameters of Z_{C_s}, we can define a velocity V_f that, set as input of the slave impedance controller, produces a force equivalent to F_h.

The goal, therefore, is to find V_f such that

$$
Z_{C_s} V_f = (B_s + K_s/s) V_f = F_h.
\tag{18}
$$
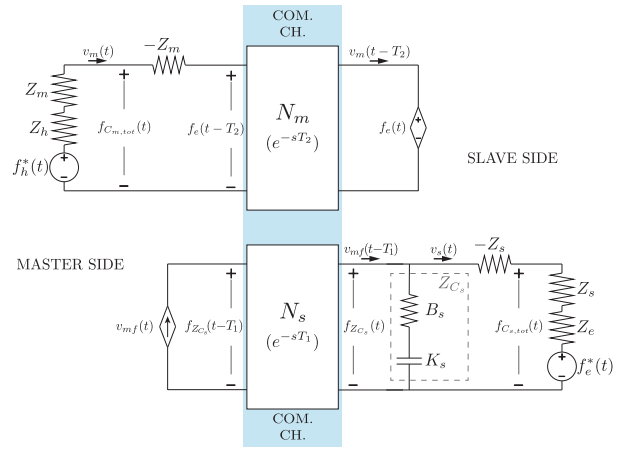
Figure 3. Circuit representation of the proposed FT^2 architecture (Fig. 2(c)).

The solution is naturally given by

$$
V_f = A_{C_s} F_h,
\tag{19}
$$

where $A_{C_s} = (B_s + K_s/s)^{-1} = Z_{C_s}^{-1}$ is an admittance controller.

Once evaluated V_f, it is possible to substitute F_h in $F_{C_s,tot}$ of (16) with its equivalent form (18)

$$
\begin{aligned}
F_{C_s,tot} &= Z_s V_s + Z_{C_s} \tilde{V}_s(t) + \overbrace{Z_{C_s} e^{-sT_1} V_f}^{\equiv e^{-sT_1} F_h} \\
&= Z_s V_s + (B_s + K_s/s)\tilde{V}_s + \underbrace{(B_s + K_s/s) e^{-sT_1} V_f}_{\equiv e^{-sT_1} F_h}.
\end{aligned}
\tag{20}
$$

Recalling that $\tilde{V}_s = e^{-sT_1} V_m - V_s$, (20) can be written as

$$
\begin{aligned}
F_{C_s,tot} &= Z_s V_s + (B_s + K_s/s)\left(e^{-sT_1} V_{mf} - V_s\right) \\
&= Z_s V_s + Z_{C_s}\left(e^{-sT_1} V_{mf} - V_s\right),
\end{aligned}
\tag{21}
$$

where $V_{mf} = V_m + V_f$. Since V_f is built to satisfy (18), the result is totally equivalent to (16), and therefore it respects transparency conditions. So, adding V_f to $V_m(t)$ and sending this sum to the slave it is possible to avoid the transmission of the measured F_h and use a two-channel architecture that respect full transparency requirements, that we call FT^2. Finally, the forces commanded to the master and slave in the FT^2 architecture, are:

$$
\begin{aligned}
F_{C_m,tot} &= Z_m V_m - e^{-sT_2} F_e, \\
F_{C_s,tot} &= Z_s V_s + Z_{C_s}\left(e^{-sT_1} V_{mf} - V_s\right).
\end{aligned}
\tag{22}
$$

The scheme relative to this solution is depicted in Fig. 2(c). Being built to be equivalent to the three-channel scheme of (16), the transmitted impedance is the same of this last.

As obvious, the lower the number of transmitted signals, the simpler the passivity layer, since we need to monitor less signals and the passivity controller is lighter. This is a significant strength of the FT^2 framework, as it will be clear in the following, comparing the passivity layer designed for the 4C and the ones designed for the FT^2 and the TIFT^2 architectures.

4   Time Domain Passivity Approach

New rising communication technologies are drastically decreasing the transmission latency. With really low delays, the stability of bilateral teleoperation systems could be better treated. However, as long as these new technologies are not able to assure a bandwidth large enough to critically decrease the latencies, a stability layer has to be designed. Here, we propose the application of the Time Domain Passivity Approach to the proposed architecture.

As already said in the introduction, the TDPA has been presented in Hannaford and Ryu (2002), and then applied to different scenarios, as position-position (Artigas et al. 2010) and four-channel frameworks (Rebelo and Schiele 2015; Artigas et al. 2016), to assure stability through passivity regardless the communication delay. As introduced in Hannaford and Ryu (2002), this approach is based on the passivity condition of the energy fluxes through a given *n*-ports network:

$$E_N(k) = \sum_{i=1}^{n} E_i(k) = \sum_{i=1}^{n} \sum_{j=0}^{k} f_i(j)v_i(j) \geq 0, \forall k \geq 0, \quad (23)$$

where N is the n-port network block, $E_i(k)$ is the total energy passed through the i-th port at the k-th step, that is defined as the integral of the power associated to that port, given by the product of associated force $f_i(k)$ and velocity $v_i(k)$. The condition (23) is constantly monitored by a Passivity Observer (PO) and if not respected it causes the activation of the Passivity Controller (PC), that damps one of the variables associated to one port, depending on the port of interest and its causality, to drain the excessive energy. Therefore, the causality of the port establishes the form of the PC, that can then be in impedance or admittance form (acting on the force or on the velocity, respectively). In this paper only the impedance form is used, for reasons explained later. To have an insight of both types, please refer to Hannaford and Ryu (2002). The impedance form PC is equivalent to a series variable resistor α_{PC}, tuned to inject energy in the net with the following law:

$$\alpha_{PC}(k) = \begin{cases} \frac{-E_{PO}(k)}{\Delta T v^2(k)}, & \text{if } E_{PO}(k) < 0, v(k) \neq 0 \\ 0, & \text{if } E_{PO}(k) > 0 \end{cases}, \quad (24)$$

where ΔT is the step time of the controller and $E_{PO}(k)$ is the energy observed by the PO at k-th step, equivalent to the sum of (23) and the energy introduced by the PC

$$E_{PO}(k) = E_N(k) + \Delta T \sum_{j=1}^{k} \alpha_{PC}(j-1)v^2(j-1) \quad (25)$$
$$= E_N(k) + E_{PC}(k-1),$$

where E_{PC} is the energy introduced by the PC and is delayed by one step because, in the control cycle, passivity action can be done only after the evaluation of E_N and so it is available to the PO with a one step delay. The force produced by the PC is

$$f_{PC}(k) = \alpha_{PC}(k)v(k). \quad (26)$$

As originally presented in Hannaford and Ryu (2002), it is appropriate to use the equivalent circuit representation of the system on which the TDPA has to be applied. This because the network ports and their associated variables in this representation are well explicited. Furthermore, Artigas et al. (2010) introduced the Time Delayed Power Network (TDPN) to represent and include in the circuit equivalent the presence of the delay in an energy consistent way. TDPNs have been used also in Rebelo and Schiele (2015) and Artigas et al. (2016). Here the same tool is applied to the proposed FT^2 scheme (Fig. 2(c)) and the result is depicted in Fig. 3. N_m is the TDPN at the master side that represents the delay T_1 of the environment force $f_e(t)$ sent from the slave to the master (and indeed it is at the left of N_m, at the slave side), while N_s is the TDPN corresponding to the delay T_2 during the communication of the augmented master velocity $v_{mf}(t)$ to the slave side. Note that the admittance controller A_{C_s} of Fig. 2(c) at the master side, that converts F_h in V_f then added to V_m to create V_{mf}, is not depicted in Fig. 3. Instead, all this process in implicitly included in the dependent current generator $v_{mf}(t)$, depicted at the left (master) side of N_s. The force $f_{Z_{C_s}}(t)$ is generated by the controller Z_{C_s}, at the slave side, whose branch is then represented at the left side of N_s. The variables associated with their left and right ports are

$$N_m : \begin{cases} < f_e(t-T_2), v_m(t) > & \text{left} \\ < f_e(t), v_m(t-T_2) > & \text{right} \end{cases}$$
$$N_s : \begin{cases} < f_{Z_{C_s}}(t-T_1), v_{mf}(t) > & \text{left} \\ < f_{Z_{C_s}}(t), v_{mf}(t-T_1) > & \text{right} \end{cases} \quad (27)$$

Note that, differently from a classic position-force architecture (see Artigas (2014)), the velocity associated to the ports of N_m is not the same of N_s. This because, in order to respect full transparency, the framework loses its "symmetry": at the master side, f_e is the force received from the slave and applied to the master end effector, which moves at a velocity v_m, that is also the velocity of the human. At the slave side, instead, the velocity received is the "augmented" one v_{mf}, different from v_m as needed to respect transparency conditions.
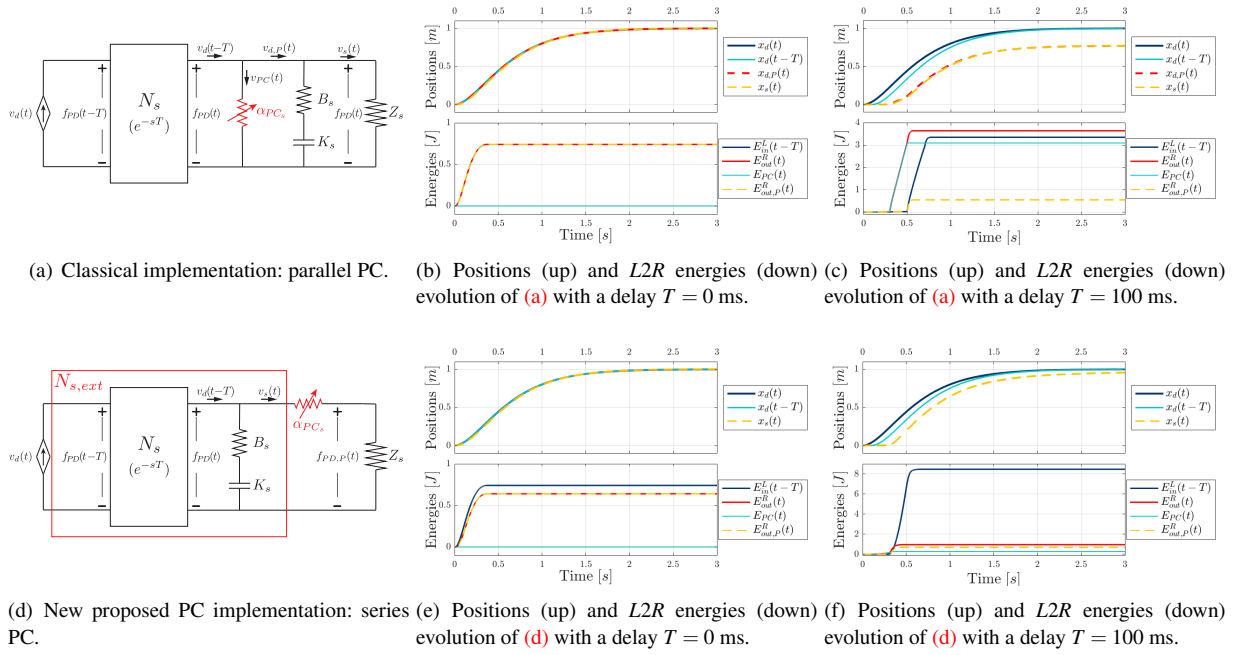
Note also that in case $T_1 \neq T_2$, the observable variables at the left port of N_m and at the right port of N_s are not the ones of (27). Indeed, regarding the right port of N_m, v_m is sent from the master to the slave side. The forward channel has a delay of T_1, so v_m will be received at the right side with a delay of T_1 and not T_2. The same reasoning can be applied to $f_{Z_{C_s}}$ of the N_s left port. It is then appropriate to define two new networks, called *observable networks*, N_m^{obs} and N_m^{obs}, whose port variables are

$$N_m^{obs} : \begin{cases} < f_e(t-T_2), v_m(t) > & \text{left} \\ < f_e(t), v_m(t-T_1) > & \text{right} \end{cases}$$
$$N_s^{obs} : \begin{cases} < f_{Z_{C_s}}(t-T_2), v_{mf}(t) > & \text{left} \\ < f_{Z_{C_s}}(t), v_{mf}(t-T_1) > & \text{right} \end{cases} \quad (28)$$

4.1   A detailed TDPC application to avoid position drift in position-based controls

As done in all the previous applications of this approach, each TDPN should be matched with a dedicated PO and PC, in a form that depends on the causality of the ports: impedance form (series PC) if the causal variable is a force, admittance form (parallel PC) otherwise. So, a series PC

(a) Classical implementation: parallel PC.

(b) Positions (up) and *L2R* energies (down) evolution of (a) with a delay $T = 0$ ms.

(c) Positions (up) and *L2R* energies (down) evolution of (a) with a delay $T = 100$ ms.

(d) New proposed PC implementation: series PC.

(e) Positions (up) and *L2R* energies (down) evolution of (d) with a delay $T = 0$ ms.

(f) Positions (up) and *L2R* energies (down) evolution of (d) with a delay $T = 100$ ms.

Figure 4. *L2R* energy fluxes of a simple trajectory following in free motions relative to the two solutions for the passivisation of a TDPN with admittance causality (N) followed by a PD control (RC net). First row: (a) circuit representation of the classic solution with a parallel PC and the simulated evolution of positions and energies with (b) $T = 0$ ms and (c) $T = 100$ ms. Second row: (d) circuit representation of the implemented free position drift solution with a series PC (extended observed net $N_{s,ext}$ in red) and evolution of positions and energies with (e) $T = 0$ ms and (f) $T = 100$ ms. The simulation parameters are: $Z_s = M * s^2 + B * s$, with $M = 1$ Ns^2/m and $B = 0.1$ Ns/m, and $K_s = 50$ N/m, $B_s = 10$ Ns/m. .

is required at the master side, while the slave side needs a parallel one. The problem of the parallel PC is that it would damp the received velocity $v_{mf}(t - T_1)$, used right after in the impedance controller net Z_{C_s} (see Fig. 3). Z_{C_s} includes an integration of $\tilde{v}_s(t) = v_{mf}(t - T_1) - v_s(t)$ (the capacitor K_s) and then, the integration of the damped (passivated) v_{mf} (namely $v_{mf,P}$) would lead to a wrong position tracking (an unpredictable drift between the master and the slave position). A first solution is presented in Artigas (2014), where in case of passive behavior (so for that instant in which (23) holds) the excess energy is used to recover this drift. Even so, this solution can't assure the perfect recovery (i.e. if the excess energy is not enough for this action). A second solution is proposed in Chawda et al. (2014), in which the drift compensation is always assured. However, this solution is not convenient for our application, as it will be clarified in Subsection 5.2.

A third solution was firstly presented in Ryu and Preusche (2007), later adopted also in Panzirsch et al. (2013) and Laghi et al. (2017). In this case, the observed network is extended(then called $N_{s,ext}$) including also the impedance controller (here Z_{C_s}) branch (see Fig. 4(d)). Consequently, the causal variable of the left port becomes $f_{Z_{C_s}}(t)$ and it is possible to use a series PC leaving $v_m(t - T_1)$ untouched, so to have the integral action always pushing to reach the right position despite passivisation actions. Fig. 4 depicts and compares the evolution of positions and *L2R* energy fluxes at the slave side of the classic solution (Fig. 4(a)) with the latter (Fig. 4(d)) for delays $T = 0$ and $T = 100$ ms. Only the *L2R* energies are considered because at the left side of N_s there is an ideal dependent current source, which absorbs any amount of energy (see, e.g., Rebelo and Schiele (2015)

for an extensive explanation). Please, refer to the next section and Artigas et al. (2010) for the definition of the analyzed energy fluxes. In the $T = 0$ case (Fig. 4(b) and (e)) both the solutions do not passivate $E_{out}^R(t)$ (i.e. $E_{PC}(t) = 0 \forall t \geq 0$) and the slave position $x_s(t)$ always follows the desired one, $x_d(t)$. In the delayed case ($T = 100$ ms), the classical solution (Fig. (c)), intervening directly on the received $v_d(t - T)$, gives to the PD controller a damped/passivated $v_{d,P}(t)$ inhibiting the slave to reach the desired position. On the contrary, with the new solution the passivated variable is the force produced by the PD $f_{PD}(t)$. The effect is just a damped trajectory of the slave that, at the end, reaches the desired position $x_d(t - T)$ (see Fig. (f)). Note that with the new solution E_{out}^R is lower that the classical one, thanks to the compensator K_s of the control net that stores some energy and creates this effect (i.e., dumps E_{out}^R). As consequence, from (23), the system results more robust in the passivity condition with respect to communication delays. This is particularly visible comparing the energy plots of (b) and (e). Moreover, this solution does not need any additional compensation, as in Artigas (2014), keeping the system simple.

A possible further improvement can be performed taking into account the efficiency of the energy dissipation, which however is not the aim of this paper. An interesting work in this direction can be found in Panzirsch et al. (2019), in which the authors analyze the excessive conservatism of the solution just described, when applied to a particular framework (the two-channel Position-Force computed). Then, they propose a solution that, considering the energy reflection of the storage element, tries to reduce the conservatism with a smart distribution of the energy dissipation. Even if applied to a rather different framework
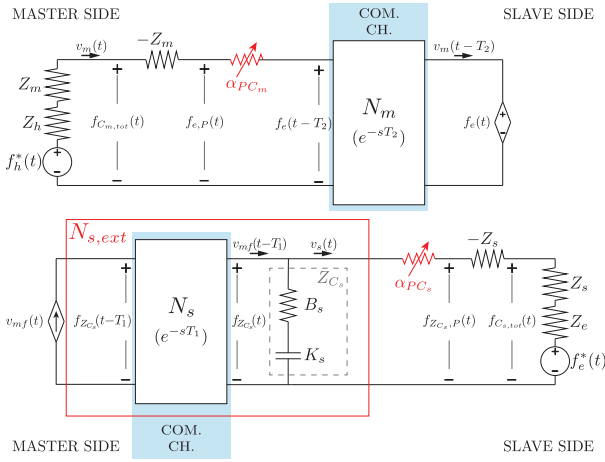
Figure 5. Circuit representation of the proposed FT^2 architecture (Fig. 2(c)) with extended observed net at slave side ($N_{s,ext}$) and passivity controllers α_{PC_m} and α_{PC_s} (red highlighted resistors).

(which does not assure transparency and can suffer from the phantom force effect), the proposed approach is promising. Its design for the FT^2 architecture introduced here is left for future work of to the readers interested in efficient passivisation, which is not the main goal of the present paper.

4.2 Time Domain Passivity Control for the proposed FT^2 Architecture

The electric equivalent of FT^2 framework including the extended observed network and the passivity controller resistors, is depicted in Fig. 5. The variables associated to the ports of $N_{s,ext}$ are

$$N_{s,ext} : \begin{cases} < f_{Z_{C_s}}(t - T_1), v_{mf}(t) > & \text{left;} \\ < f_{Z_{C_s}}(t), v_s(t) > & \text{right,} \end{cases} \quad (29)$$

while, as explained previously, the ones of the observable network $N_{s,ext}^{obs}$ are

$$N_{s,ext}^{obs} : \begin{cases} < f_{Z_{C_s}}(t - T_2), v_{mf}(t) > & \text{left;} \\ < f_{Z_{C_s}}(t), v_s(t) > & \text{right.} \end{cases} \quad (30)$$

The energy observed by the master and slave POs are

$$E_{PO_m}(k) = E_{N_m,\text{obs}}^{R2L}(k) + E_{PC_m}(k-1); \\ E_{PO_s}(k) = E_{N_{s,ext},\text{obs}}^{L2R}(k) + E_{PC_s}(k-1), \quad (31)$$

where apex *R2L* and *L2R* stands for *right-to-left* and *left-to-right*,respectively, with

$$E_{N_m,\text{obs}}^{R2L}(k) = E_{N_m^{obs}}^{R,in}(k - T_2) - E_{N_m^{obs}}^{L,out}(k); \\ E_{N_{s,ext},\text{obs}}^{L2R}(k) = E_{N_{s,ext}^{obs}}^{L,in}(k - T_1) - E_{N_{s,ext}^{obs}}^{R,out}(k), \quad (32)$$

where $E_{N_m^{obs}}^{R,in}$ and $E_{N_{s,ext}^{obs}}^{L,in}$ are delayed because observed at one side of the network and then sent to the other. In these last apex, L and R indicate for the left and right ports, while *in* and *out* indicates the energy flows in and out that port,
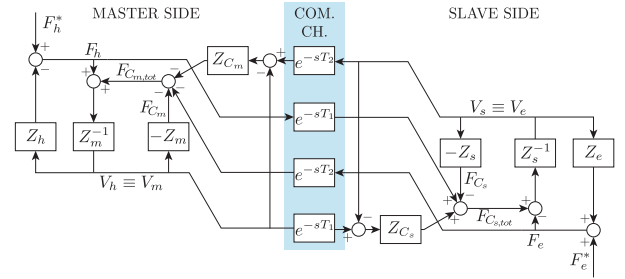
respectively

$$E^{*,in}(k) = \sum_{i=0}^{k} P^{*,+}(i); \\ E^{*,out}(k) = \sum_{i=0}^{k} P^{*,-}(i), \quad (33)$$

where

$$P^{*,+}(k) = f(k)v(k) \quad \text{iff} \quad f(t)v(t) > 0, \forall k \geq 0; \\ P^{*,-}(k) = -f(k)v(k) \quad \text{iff} \quad f(t)v(t) < 0, \forall k \geq 0, \quad (34)$$

with f and v being the force and velocity associated to the port $*$. $P_{N_m^{obs}}^L$, $P_{N_m^{obs}}^R$, $P_{N_s^{obs}}^L$ and $P_{N_s^{obs}}^R$ can be easily defined

(a) Block diagram representation of the four-channel architecture corresponding to (13).
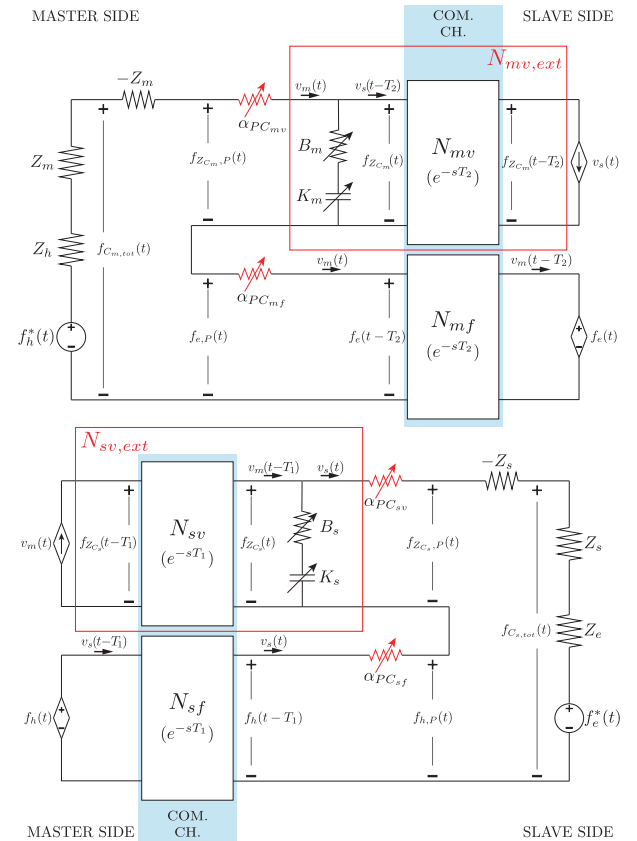
(b) Circuit representation of the four-channel architecture corresponding to (13), comprehensive of passivity controllers and extended observed nets at the master and slave sides highlighted ($N_{mv,ext}$ and $N_{sv,ext}$ respectively).

Figure 6. Block diagram representation (a) and electric equivalent (b) of the four-channel architecture corresponding to (13).

multiplying the relative conjugate port variables defined in the first bracket of (28) and (30). Please, refer to Artigas et al. (2010) for a detailed derivation of the previous equations. Since two are the communicated signals (v_{mf} from master to slave and f_e from slave to side), two are also the PCs used to assure the passivity of the framework, one at each side (α_{PC_m} and α_{PC_s}), as visible in Fig. 5. From (24), the specific law regulating these two PCs are

$$\alpha_{PC_m}(k) = \begin{cases} \frac{-E_{PO_m}(k)}{\Delta T v_m^2(k)}, & \text{if } E_{PO_m}(k) < 0, v_m(k) \neq 0 \\ 0, & \text{if } E_{PO_m}(k) > 0 \end{cases}; \quad (35)$$

$$\alpha_{PC_s}(k) = \begin{cases} \frac{-E_{PO_s}(k)}{\Delta T v_s^2(k)}, & \text{if } E_{PO_s}(k) < 0, v_s(k) \neq 0 \\ 0, & \text{if } E_{PO_s}(k) > 0 \end{cases}, \quad (36)$$

with E_{PO_m} and E_{PO_s} given by (31). As visible from these equations, α_{PC_m} is regulated also in function of v_m, and α_{PC_s} in function of v_s. The energy introduced in the network by the passivity controllers, E_{PC_m} and E_{PC_s}, taken into account in (31) in the calculation of E_{PO_m} and E_{PO_s}, are

$$E_{PC_m}(k) = \Delta T \sum_{j=1}^{k} \alpha_{PC_m}(j)v_m^2(j);$$
$$E_{PC_s}(k) = \Delta T \sum_{j=1}^{k} \alpha_{PC_s}(j)v_s^2(j). \quad (37)$$

Finally, the variable revised by the PC at the master side is the one received from the slave f_e

$$f_{e,P}(t) = f_e(t - T_2) - f_{PC_m}(t)$$
$$= f_e(t - T_2) - \alpha_{PC_m}(t)v_m(t), \quad (38)$$

where $f_{e,P}$ is the result of the passivisation action and $f_{PC_m}(t) = \alpha_{PC_m}(t)v_m(t)$ is force produced by PC_m (see Fig. 5). In a similar way, the variable revised at the slave side is the on produced by the impedance controller $f_{Z_{C_s}}$

$$f_{Z_{C_s},P}(t) = f_{Z_{C_s}}(t) + f_{PC_s}(t)$$
$$= f_{Z_{C_s}}(t) + \alpha_{PC_s}(t)v_s(t), \quad (39)$$

where, again, $f_{Z_{C_s},P}$ is the result of the passivisation and $f_{PC_s}(t) = \alpha_{PC_s}(t)v_s(t)$ is force produced by PC_s. Note that f_{PC_m} is subtracted in (38), while f_{PC_s} is added in (39). This is due to the network causality and the "direction" of the passivisation.

In the experimental section, the new proposed architectures will be tested using as benchmark the four-channel corresponding to (13), for which the passivity controllers are implemented following the solution presented in Subsection 4.1. For sake of clarity, its block diagram and electric equivalent are depicted in Fig. 6(a) and Fig. 6(b), respectively. In this case, the passivated variables are four (as the number of transmitted signals): $f_{Z_{C_m}}(t)$ and $f_e(t - T_2)$ at the master side, and $f_{Z_{C_s}}(t)$ and $f_h(t - T_1)$. The laws regulating these passivisations are leaved to the reader, as they can be easily derived from the previous equations.

5 Fully transparent two-channel architecture with tele-impedance

Once defined the FT^2 architecture, one big issue can be raised regarding the choice of the gains K_s and B_s of the slave impedance controller Z_{C_s}.

When no communication delay is present (i.e. $T_1 = T_2 = 0$s) any choice is ideally fine, since the scheme itself already ensures full transparency. However low gains are not a good choice since, as already said, dynamic and friction compensations are never perfect: if low K_s and B_s are used, a relevant position tracking error in steady state will always occur. Furthermore, from (17) we saw that the higher these gains are, the closer the transmitted impedance is to the ideal one of (6).

When a delay occurs in the transmission of the signals, the choice of the impedance parameters can strongly influence the behavior of the system. In high dynamic scenarios, high gains will produce a large force $f_{Z_{C_s}}$ that corresponds to the injection of a large amount of energy in the system that, depending of its direction (referred to (33)), can threaten the passivity of the channel and provoke the action of the Passivity Controller. Much more relevant, more the delay is consistent more the framework is far from the ideal (undelayed) transparency. At the master side, the user simply receives the feedback delayed, resulting in a distorted perception of the remote interaction. At the slave side the situation is a bit more complicated. Indeed, when no delay is present the slave reacts to any interaction with the environment exactly as the user, thanks to the transparency. This behavior, copy of the user's, is the result of a control action that embeds the user's impedance (F_h in all the scheme presented is the sum of F_h^* and $Z_h V_h$).

As well known (Ajoudani 2016), humans are able to change their limb impedance through the contraction of the muscles and use it to properly adapt to or anticipate any interaction. When a delay is present, this kind of behavior and intrinsic impedance adjustment is delayed and can also lead to a dangerous situation. For example, if an object is approaching the slave and the delay is high, in case the impedance controller is set to be very stiff an high impact will occur at the slave side, which could damage both the slave and the object. Furthermore, a high force would be fed back delayed to the user that if is not expected could lead to an injury. These considerations rise the need of an explicit adjustment of the slave impedance controller gains so to duplicate as close as possible the ones of the human, despite any delay. To achieve this, Tele-Impedance framework (Ajoudani et al. 2012) can be exploited, as explained in the following subsections.

5.1 Tele-impedance control: State of the Art

Tele-impedance (Ajoudani et al. 2012) is a control paradigm developed in the last five years. It consists in teleoperating a robot through an impedance controller by measuring and replicating the user's limb pose and impedance on the slave robot in real-time. The user's impedance is estimated by monitoring the muscles' activity through the use of surface electromyography (sEMG) and interpreted to estimate the impedance of the human limb.

Towards the tracking of the human physical interaction behaviour in 3D space using a principled simplification approach, recently (Ajoudani et al. 2017; Fang et al. 2018), the tele-impedance concept is extended based on the dependency of the arm endpoint stiffness to both geometric human arm configuration (Configuration

Dependent Stiffness - CDS) and muscular activity (Common Mode Stiffness - CMS).

CDS includes the effect of arm configuration and muscle moment arms that contribute to the variations in the geometry of the arm endpoint stiffness. The tracking of the arm kinematics is achieved through passive marker motion capture system using the concept of arm tangle, as explained in Fang et al. (2018). Three rigid-body markers can be attached to the hand, elbow and shoulder segments and used for the tracking of the arm Jacobian ($J_a(q_a)$), with $q_a \in \mathbb{R}^7$ being the arm joint angles. Using the muscle attachment points, and the length variations over the joint angles, i.e. the muscle Jacobian ($J_{musc}(q)$) can be computed online (Ajoudani et al. 2017).

CMS, on the other hand, implements a coordinated co-activation of the arm muscles, while its tracking is achieved by a co-contraction index (a_{cc}), calculated from the dominant and easily accessible muscles of the arm for surface electromyography measurements (u, i.e., the filtered and normalised EMG signals of the muscles), i.e. the Biceps Brachii (BB) and Triceps Brachii (TB), as $a_{cc} = \frac{u_{BB}+u_{TB}}{2}$. This index provides a rough estimate of the arm muscles' co-activation pattern. Through a pre-defined muscle synergy matrix (K_{syn}), this index contributes to modifications in the volume of the endpoint stiffness ellipsoid.

Finally, the congruence conservative transformation from the joint space to the Cartesian space of the human arm can be written to obtain the estimated endpoint stiffness $\hat{K}_h$ (see

Figure 8. Overall block representation of TIFT[2] on the real setup, comprehensive of CMS-CDS tele-impedance and Passivity Observers and Controllers.

details in Ajoudani et al. (2017))

$$\hat{K}_h = J_a^{+T}(q_a) \left[J_{musc}^T(q_a) a_{cc} \, K_{syn} J_{musc}(q_a) \right] J_a^+(q_a). \quad (40)$$

The damping matrix of the human arm $\hat{B}_h$ can be obtained from $\hat{K}_h$ following the damping design in Albu-Schaffer et al. (2003) as

$$\hat{B}_h = 2\xi \bar{K}_h^{1/2}, \quad (41)$$

where $\bar{K}_h$ includes only the diagonal elements of $\hat{K}_h$, and ξ is the desired damping ratio. The diagonal consideration has been taken into account for the sake of simplicity.

The force commanded to the robot arm is

$$F_c(s) = e^{-sT_1}\hat{Z}_h(s)\tilde{V}_s = e^{-sT_1}\left(\hat{B}_h(s)\tilde{V}_s + \hat{K}_h(s)\tilde{X}_s\right), \quad (42)$$

where $\hat{Z}_h(s)$ is the estimated human endpoint impedance, T_1 is the transmission delay, $\tilde{X}_s = e^{-sT_1}X_m - X_s$ and $\tilde{V}_s = e^{-sT_1}V_m - V_s$, with X_m, X_s and V_m, V_s that are the master/human and slave positions and velocities, respectively.

5.2 Fully transparent two-channel architecture augmented with tele-impedance

As explained above, the tele-impedance control sends to the slave robot just the position of the user arm and its estimated impedance (stiffness) and doesn't foresee any feedback to the user, being a unilateral tele-manipulation control. In our previous work (Laghi et al. 2017) a force feedback is provided, creating a two-channel bilateral tele-manipulation framework, called tele-impedance with Force-Feedback (TIFF). Compared with the analysis above regarding the alternatives for complete transparency, its easy to see that TIFF of Laghi et al. (2017) doesn't respect full transparency requirement. Indeed, it doesn't include the third channel of Fig. 2(b) nor the admittance control (19) that maps F_h into V_f of Fig. 2(c).

(a) Block Representation of the TIFT[2] scheme.

(b) Electric equivalent of the TIFT[2] scheme.

Figure 7. Representation of the proposed fully transparent two-channel architecture augmented with tele-impedance TIFT[2]: (a) block scheme and (b) electric equivalent with master and slave *PC*s.

The easiest way to obtain a framework that contains the tele-impedance paradigm and shows full transparency is the substitution of the slave impedance controller Z_{C_s} of FT^2 (Fig. 2(c) and (22)) with the estimated human impedance $\hat{Z}_h$ (42). Since tele-impedance is a variable impedance control, some additional signals have to be sent to the slave, i.e. the estimated human impedance parameters. From (41), once ξ is chosen, $\hat{B}_h$ is defined only through $\hat{K}_h$, so it is enough to send this last one and embed the proportion (41) at the slave side.

Furthermore, also A_{C_s} has to be modified, to include the variable gains. In particular it has to be substituted with the human admittance $\hat{A}_h$, that from (42) results

$$\hat{A}_h(s) = \hat{Z}_h^{-1}(s) = \left(\hat{B}_h(s) + \frac{\hat{K}_h(s)}{s} \right)^{-1}. \tag{43}$$

In this case, the relation (19) becomes

$$V_f(s) = \hat{A}_h(s) F_h(s). \tag{44}$$

The inclusion of the tele-impedance control in the FT^2 scheme of Fig. 2(c) as explained now generates a new framework, the TIFT^2. The block and circuit equivalent schemes of TIFT^2 are depicted in Fig. 7(a) and Fig. 7(b), respectively. Fig. 8 depicts a graphic general scheme, comprehensive of the passivity layer blocks.
The resulting forces commanded to master and slave are

$$
\begin{aligned}
F_{C_m,tot} &= Z_m V_m(t) - e^{-sT_2} F_e, \\
F_{C_s,tot} &= Z_s V_s + e^{-sT_1} \hat{Z}_h (e^{-sT_1} V_{mf} - V_s(t)) \\
&= Z_s V_s + e^{-sT_1} \left(\hat{B}_h + \frac{\hat{K}_h}{s} \right) \left(e^{-sT_1} V_{mf} - V_s(t) \right).
\end{aligned}
\tag{45}
$$

It is important to underline that, since no (temporal) constrains are given on the choice of the local controllers by the transparency conditions (9), and since TIFT^2 is directly derived from FT^2 (that has been built to respect transparency requirements), it follows that TIFT^2 automatically respects transparency conditions as well. Note that even if the total signal transmitted to the slave are now three ($\hat{K}_h$ wasn't present in the original 2-channel scheme of Fig. 2(c)), the network observed at the slave side continues to be a two-port (Fig. 7(b)).

The design of the TDPC for the TIFT^2 is exactly the same performed for the FT^2 in Subsec. 4.2, substituting $f_{\hat{Z}_h}(t)$ to $f_{Z_{C_m}}(t)$. Furthermore, being the impedance branch $\hat{Z}_h$ already included in the extended observed network $N_{s,ext}$, the energy introduced in the system by the impedance gains variation is automatically observed and passivated. This is really important for the system stability: since $\hat{Z}_h$ varies in accordance to the user impedance, sudden changes in $\hat{K}_h$ can occur. These changes could result in a non-passive behavior and can lead to instability. This issue is, basically, the same happening at the user side in MMT applications (see Section 2) due to the update of the local environment model. The inclusion of $\hat{Z}_h$ in the observed network automatically avoid this risk and doesn't need a more specific handling of the system stability. This would have not been possible, naturally, if the drift compensation solutions proposed in Artigas (2014) and Chawda et al. (2014) were adopted instead of the one in Laghi et al. (2017).
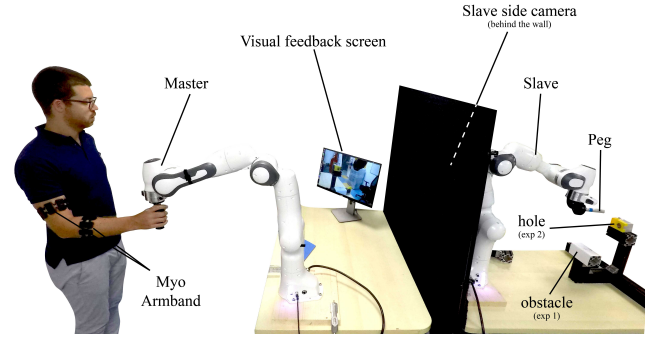
Figure 9. Experimental setup with the Panda robotic arms, used for the multi-subject experiments.

6 Experiments

6.1 Experimental Setup

The master-slave framework used for the validation of the proposed architecture is implemented using as master-slave system composed by two Panda arms, by Franka Emika. Fig. 9 shows the full setup. The slave end-effector is a simple peg with a length of 130 mm a diameter of 25 mm. A wall is put between the master and the slave, to prevent the user to directly look at the slave side. Instead, a camera shoots the slave scene and the images are projected to a screen. This allows to delay the visual feedback synchronously with the force feedback and recreate a scenario closer to a real one. The auditive feedback is instead removed using noise canceling headphones and white noise.

The control architecture is split in two threads, one for the master and one for the slave, both running on the same machine at 1 KHz. The communication channels are implemented using a shared data structure between the two threads and the desired delay is simulated through properly dimensioned data buffers. The master and slave positions are provided by the software library interface of the robots (Franka Research Interface, FCI), while human and environment wrenches (F_h and F_e, respectively) are sensed through the external estimated joint torques τ^{ext}, provided by the external torque observer of the robot controllers:

$$F_h = J_m^{+T} \tau_m^{ext}; \tag{46}$$

$$F_e = J_s^{+T} \tau_s^{ext}, \tag{47}$$

where $F_* = [f_*^T \ \tau_*^T]^T$ is the wrench vector, with $f = [f_*^x \ f_*^y \ f_*^z]^T$ the forces vector and $\tau_* = [\tau_*^x \ \tau_*^y \ \tau_*^z]^T$ the torques vector in the end-effector (Cartesian) frame, J is the robot geometric Jacobian matrix and J^+ is its pseudo-inverse.

The estimation of human impedance parameters of Sec. 5.1 is implemented as follows. The muscle activity and the user's arm segment orientations are calculated using the commercialized wearable Myo Armbands (Thalmic Labs, Inc.). These armbands embed eight EMGs and an IMU, that provides the rotational quaternion, each.
Two Myos are worn by the user, one at the upper arm and one at the forearm, which provide the quaternions of these two segments. The hand is considered attached to the Panda master end-effector. Then, the hand rotational quaternion is calculated from the homogeneous transformation matrix of the latter. Knowing a priori the length of the user's arm

segments (upper arm, forearm and hand), it is then possible to reconstruct the arm triangle to calculate human arm and muscle Jacobians (Ajoudani et al. 2017).

The Myo signals are received by a dedicated software thread, processed and then sent to the master one at a frequency of 50 Hz. The processing of the EMG signals (filtering and normalization to maximum voluntary contraction (MVC)) is performed on-line.

Our real-time model enables the master to modify the direction of the endpoint stiffness ellipsoid by changing the arm posture in an intuitive manner, while being capable of adjusting its volume by increasing the co-contraction of the dominant arm muscles. As a result, teleoperated tasks which requires significant modulation of the endpoint stiffness and force can be executed effectively and naturally.

In the experimental section three different control architectures are considered:

i) the four-channel architecture of Fig. 6 (from now on referred as 4C);

ii) the proposed fully transparent two-channel architecture of Fig. 2(c) (FT^2);

iii) the one including tele-impedance control of Fig. 7 ($TIFT^2$).

For the 4C and FT^2 the slave stiffness matrix K_s is set as

$$K_s = \begin{bmatrix} K_l & 0 \\ 0 & K_o \end{bmatrix} \qquad (48)$$

with $K_l = diag[400 \quad 400 \quad 400]$N/m and $K_o = diag[5 \quad 5 \quad 5]$Nm/rad. These fixed values of K_l are in the middle of the range of human rendered stiffnesses (Ajoudani 2016) and large enough to compensate for modeling uncertainties and friction. For $TIFT^2$, the algorithm of Ajoudani et al. (2012) is developed only for the linear stiffness K_l. Then, the linear relation $K_o = K_l/80$ is chosen to keep the same proportion used in the 4C and FT^2 cases. The slave damping matrix B_s is instead designed imposing the critically damping factor $\xi = 0.7$.

The passivity controllers are implemented including also a rate-limiter of F_{PC}, in order to avoid strong cuts of the commanded wrench and increase the comfort and usability of the system, especially at the master side. The rates are experimentally set at 100 N/s for the forces and 1 Nm/s for the torques and their effects are considered in the E_{PC} of (31).

The setup explained above is designed to test the approach on 10 healthy subjects. Moreover, to prove the portability of the proposed architecture to different setups involving torque controlled robotic arms, the master-slave system is recreated also on two KUKA LWR4+ (Fig. 10), which is used only by one subject and showed in the video Extensions of this paper. As shown in Fig. 10, this second setup differs from the first one not only in the used robotic arms, but also in the system used for the human pose and impedance calculation. Indeed, in this case the EMG signals are acquired by the wireless Delsys Trigno system (Delsys Inc.), at 1 kHz. The tracking of the arm triangle is achieved by 11 Flex-3 cameras of the Optitrack system (NaturalPoint, Inc.) by attaching three rigid-body markers to the shoulder, elbow and wrist of the user arm, at 100 Hz. The remaining software system specifications are the same as the first setup. This second

setup is also used to develop a practical showcase, explained in Subsec. 7.4.

6.2 Experiments

We have defined two types of experiments to evaluate:

1. the transparency of the proposed solutions (FT^2 and $TIFT^2$) with no delays;

2. the advantages of the new implementation of the TDPC;

3. the removal of phantom forces and its effects on the user experience;

4. the advantages given by tele-impedance paradigm both in simple and complex interactions with the remote environment in presence of communication delays.

The first experiment, called 'Contact Recognition and Reaction', is to evaluate all the first three aspects listed above and the simple interaction case of the fourth. The second experiment is a classic peg in hole, mainly used to evaluate the third point above (phantom forces removal) and the complex interaction case of point four. Ten subjects between 25 and 37 years old conducted the experiments. The description of the two experiments and the methods used for their evaluation are described hereafter.

6.2.1 Experiment 1 - Contact Recognition and Reaction.
This experiment consists in a contact recognition and reaction task with various delays:

1. $T_1 = T_2 = 0ms$ ($T_{rt} = 0$ ms), Fig. 11(a);
2. $T_1 = T_2 = 250ms$ ($T_{rt} = 500$ ms), Fig. 11(b);
3. $T_1 = T_2 = 500ms$ ($T_{rt} = 1000$ ms), Fig. 11(c),

where $T_{rt} = T_1 + T_2$ is the round-trip delay.

In this experiment a plane obstacle is put parallel to the $x - y$ plane. The three delay profiles above are implemented in the three architecture 4C, FT^2 and $TIFT^2$. For each implementation, the subject is asked to lower the interface until he/she recognizes the contact with the obstacle, relying mainly on the haptic than the visual feedback (she/he must be certain than the contact happened). As soon as the contact is perceived, the subject is asked to react immediately by moving the slave away from the obstacle. This is repeated three times for all the architecture-delay combination. The order of the experiments is randomized w.r.t. the control
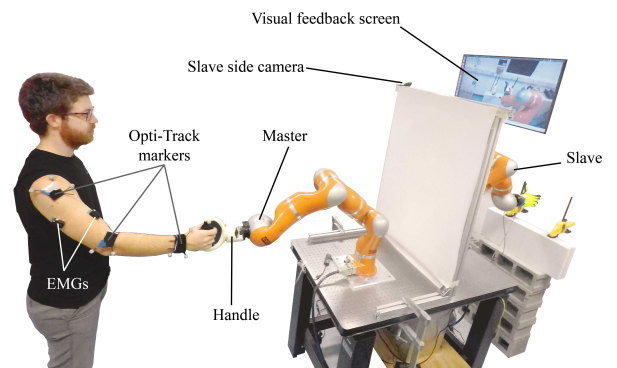
Figure 10. Setup with the two KUKA LWR4+ to show the portability of the proposed control architecture.

architecture for each subject, to avoid any learning effect, while the delays are always provided in an increasing order.

In order to compare the performances of the three architectures, two values are chosen: maximum environment interaction force along z axis $f_{e,max}^z$ and average sum of the EMG signals taken from the upper arm Myo armband $\overline{E}_{arm}$, normalized w.r.t. the 4C case. The normalization is needed because each subject has a different muscle activity level. Using the non normalized $\overline{E}_{arm}$ could then be misleading. Instead, the normalized one gives an idea of the activity w.r.t the 4C benchmark and has a better interpretation. $f_{e,max}^z$ is closely related to the stiffness along the z axis, especially when a delay is present (as a consequence of what explained at the beginning of Sec. 5). In some interaction, especially during "exploration" of the remote, possibly unknown environment, it can be desirable to lower as much as possible the forces exchanged with the environment, so to avoid any damage or unexpected consequence despite any delay. This is why this measure has been chosen as a performance index. $\overline{E}_{arm}$, instead, linked to the muscles activity, can be used as an index of the user fatigue. Lower values of $f_{e,max}^z$ and normalized $\overline{E}_{arm}$ correspond to higher performance during contact recognition and reaction.

The bar plots of Fig. 12 shows the average values $\overline{f}_{e,max}^z$ (Fig. 12(a)) and the normalized $\overline{E}_{arm}$ (Fig. 12(b)). Moreover, a statistical analysis is conducted. Since not all the data passed the Shapiro-Wilk normality test, the nonparametric Kruskal-Wallis is chosen. Table 3 reports the p-value of the statistical tests.

Furthermore, all the subjects are asked to fill out a seven-point Likert scale questionnaire after the execution of each repetition of all the architecture-delay profiles combinations. The statements of the questionnaire are listed in Tab. 2. For each statement, the possible answers range from completely disagree to completely agree, with an assigned score of 0 and 7, respectively. 0 score means better result for all the statements. The bar plots of Fig. 13 depict the average scores and standard deviations of the questionnaires for $T_{rt} = 0$ ms (Fig. 13(a)), $T_{rt} = 500$ ms (Fig. 13(b)) and $T_{rt} = 1000$ ms (Fig. 13(c)).

6.2.2 Experiment 2 - Peg in Hole. This experiment consists in a classic peg in hole task, carried out to show the advantages of real-time human like stiffness modulation in presence of delays. The peg used is a cylinder with length 130mm and diameter 25mm, while the hole has an internal diameter of 26mm and the axis parallel to x. Fig. 14 shows a frame sequence of the task executed with the

Table 2. Likert Scale Questionnaire of Experiment 1.

	Statements
E1.Q1	It was hard to use the interface to move the slave robot.
E1.Q2	It was difficult to recognize the contact.
E1.Q3	It was hard to move away from the contact.
E1.Q4	It was hard to control the system during the reaction after the contact.
E1.Q5	It was physically tiresome to accomplish the task.
E1.Q6	It was psychologically tiresome to accomplish the task.

Table 3. p-values resulting from Kruskal-Wallis test of $\overline{f}_{e,max}^z$ and normalized $\overline{E}_{arm}$ data relative to Experiment 1. Green cells correspond to p-values lower than $\alpha = 0.05$, red cells to higher p-values.

|		T_{rt}		
		0 ms	500 ms	1000 ms
$\overline{f}_{e,max}^z$	4C vs. FT^2	0.8825	0.3831	0.1171
	4C vs. TIFT^2	0.0476	0.0026	1.69e-05
	FT^2 vs. TIFT^2	0.1738	0.0187	0.0015
norm. $\overline{E}_{arm}$	4C vs. FT^2	0.1062	1.33e-04	1.33e-04
	4C vs. TIFT^2	0.4193	0.0030	1.33e-04
	FT^2 vs. TIFT^2	0.4193	0.6272	0.6911

TIFT^2. These frames are extrapolated from Extension 1, a video of the experiment to illustrate user ability to modulate robot interaction. Furthermore, Fig. 15 depicts similar results with the delay profile of $T_{rt} = 500ms$.

The modality of this second experiment is the same of Experiment 1: each subject is asked to repeat the task three times for each combination of control architecture and profile. As in the Experiment 1, the order of the experiments is randomized w.r.t. the control architecture for each subject, to avoid any learning effect, while the delays are always provided in an increasing order. This time, the performances of the schemes are evaluated through the maximum values of the interaction forces between the slave and the environment along all the axis ($f_{e,max}^x$, $f_{e,max}^y$ and $f_{e,max}^z$) during the insertion-extraction phase, as well as the average sum of the EMG signals taken from the upper arm Myo armband $\overline{E}_{arm}$, normalized w.r.t. the 4C case, as the first experiment. The bar plots of Fig. 16 show the average values $\overline{f}_{e,max}^x$ (Fig. 16(a)), $\overline{f}_{e,max}^y$ (Fig. 16(b)), $\overline{f}_{e,max}^z$ (Fig. 16(c)), and normalized $\overline{E}_{arm}$ (Fig. 16(d)), calculated between all the subjects for each delay profile. Again, a statistical analysis is conducted. As for the Experiment 1, not all the data passed the Shapiro-Wilk normality test, then the nonparametric Kruskal-Wallis is chosen. Table 5 reports the p-value of the statistical tests.

As for the first experiments, all the subjects are asked to fill out a seven-point Likert scale questionnaire after the execution of each repetition of all the architecture-delay combinations. The statements of the questionnaire are listed in Tab. 4. As for the first questionnaire, 0 score means better result for all the statements also here. The bar plots of Fig. 17 depict the average scores and standard deviations of the questionnaires for $T_{rt} = 0$ ms (Fig. 17(a)), $T_{rt} = 500$ ms (Fig. 17(b)) and $T_{rt} = 1000$ ms (Fig. 17(c)).

7 Results and discussion

The similarity of the master and slave positions in the central and left columns of Fig. 11(a) (FT^2 and TIFT^2, respectively) provides evidence on the transparency of the teleoperation control framework. Indeed, the master and slave positions are always equal, also in the contact interval (green band). Furthermore, with abuse of notation, in the second raw of the plots of Fig. 11(a), f_{C_m} indicates the total force commanded to the master without the dynamic compensation (i.e. $f_{C_m} =$
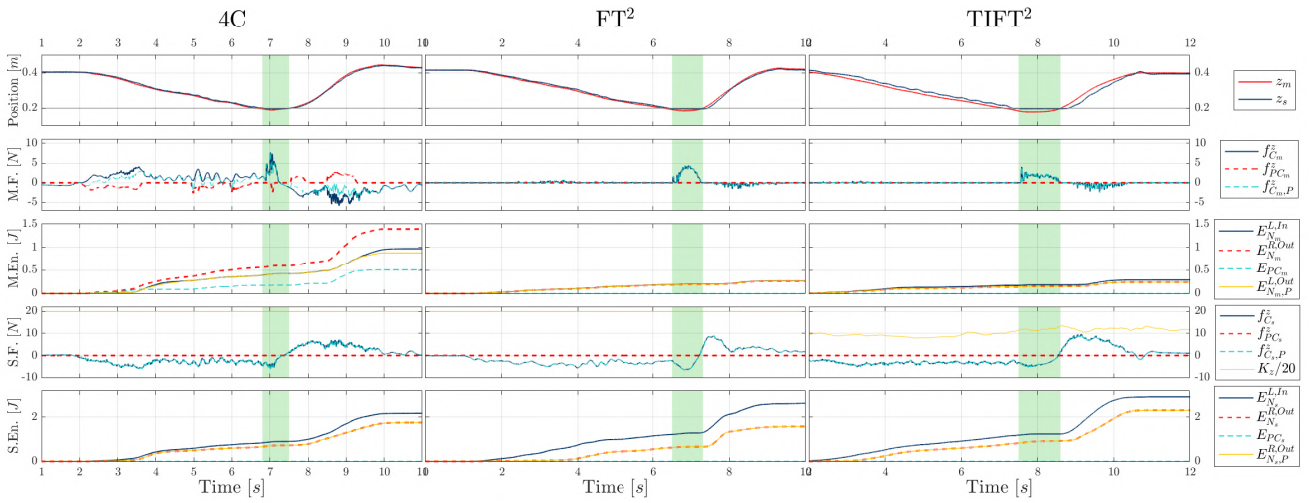
(a) Experiment 1.a ($T_{rt} = 0$ ms): four-channel (4C, left), fully transparent two channel without (FT^2, center) and with tele-impedance (TIFT^2, right).
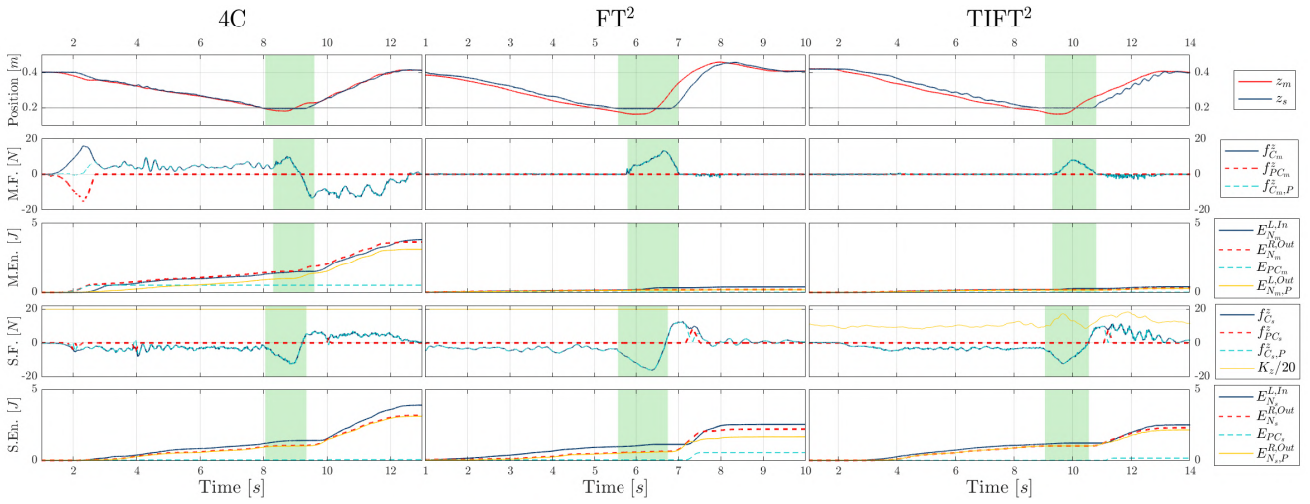

(b) Experiment 1.b ($T_{rt} = 250$ ms): four-channel (4C, left), fully transparent two channel without (FT^2, center) and with tele-impedance (TIFT^2, right).
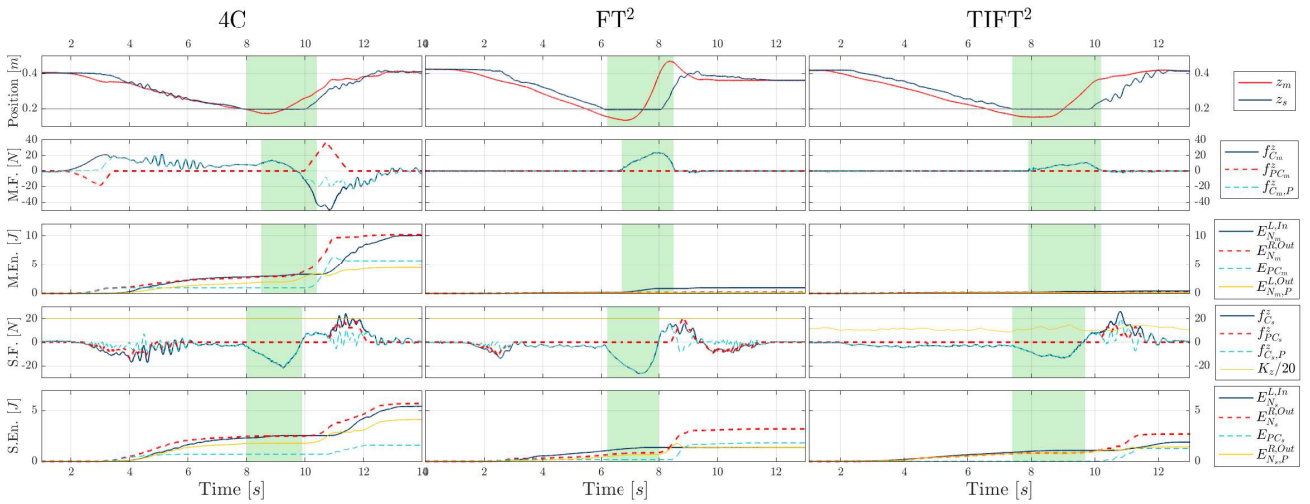

(c) Experiment 1.c ($T_{rt} = 500$ ms): four-channel (4C, left), fully transparent two channel without (FT^2, center) and with tele-impedance (TIFT^2, right).

Figure 11. Experiment 1 results: Comparison of contact recognition and reaction along z direction using the four-channel architecture (4C, left column), the proposed two-channel architecture without (FT^2, center column) and with tele-impedance (TIFT^2, right column) when channel delays are (a) $T_{rt} = 0$ ms, (b) $T_{rt} = 250$ ms, (c) $T_{rt} = 500$ ms. The green areas indicates the contact intervals. First rows: master and slave position. Second rows: master commanded force without dynamic compensation ($f_{C_m}^z(t) = f_{C_m,tot}^z(t) - f_{Z_m}^z(t)$, equal to $f_e^z(t)$ for FT^2 and TIFT^2), master passivity controller generated force $f_{PC_m}^z(t)$ and passivated force $f_{C_m,P}^z(t)$. Third rows: master energies $E_{N_m}^{R,In}(t - T_2)$, $E_{N_m}^{L,Out}(t)$, $E_{PC_m}(t)$, $E_{N_m,P}^{L,Out}(t) = E_{N_m}^{L,Out}(t) - E_{PC_m}(t)$. Fourth rows: slave commanded force without dynamic compensation ($f_{C_s}^z(t) = f_{C_s,tot}^z(t) - f_{Z_s}^z(t)$, equal to $f_{Z_{C_s}}^z(t)$ for FT^2 and $f_{Z_h}^z(t)$ for TIFT^2), slave passivity controller generated force $F_{PC_s}^z(t)$ and passivated force $f_{C_s,P}^z(t)$. Fifth rows: slave energies $E_{N_s}^{L,In}(t - T_1)$, $E_{N_s}^{R,Out}(t)$, $E_{PC_s}(t)$, $E_{N_s,P}^{R,Out}(t) = E_{N_s}^{R,Out}(t) - E_{PC_s}(t)$.
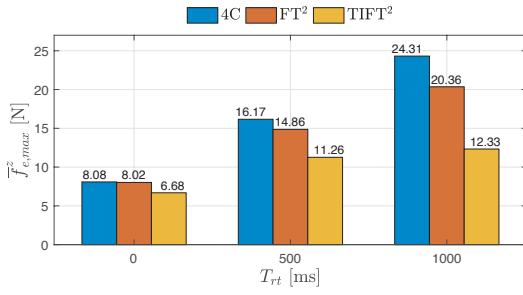
(a) Average maximum force $\overline{f}^z_{e,max}$ during contact recognition and reaction: the lower the better.
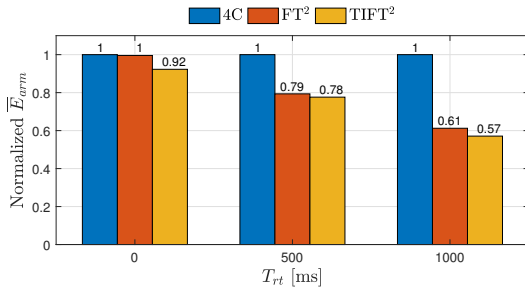
(b) Average EMGs $\overline{E}_{arm}$ normalized w.r.t. 4C case: the lower the better.
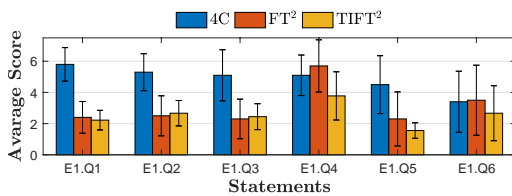
Figure 12. Performances comparison between TI, FT^2 and TIFT^2 during contact and reaction experiments. Averages values of (a) maximum contact force along z axis and (b) average EMGs normalized w.r.t. 4C case. Lower values correspond to better performances.
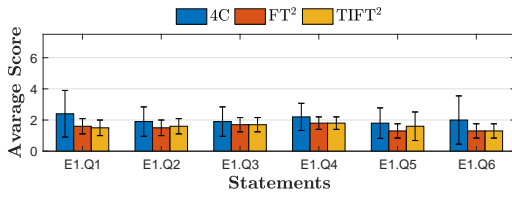
(a) $T_{rt} = 0$ ms.
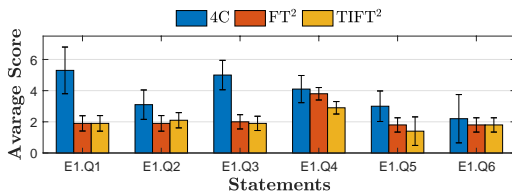
(b) $T_{rt} = 500$ ms.

(c) $T_{rt} = 1000$ ms.

Figure 13. Average scores of the statements of Experiment 1 questionnaire (Tab. 2) in (a) $T_{rt} = 0$ ms, (b) $T_{rt} = 500$ ms and (c) $T_{rt} = 1000$ ms cases.

$f_{C_{m,tot}-f_{Z_m}}$, see (16) and (45)). In the FT^2 and TIFT^2 cases, this corresponds always to f_e. This means that the force displayed to the user is always f_e. Then, since $x_s = x_m$ as shown in the plots, the impedance transmitted to

Table 4. Likert Scale Questionnaire of Experiment 2.

	Statements
E2.Q1	It was hard to use the interface to move the slave robot.
E2.Q2	It was difficult to align the peg with the hole.
E2.Q3	It was hard to insert the peg into the hole.
E2.Q4	It was hard to control the interaction during the peg insertion.
E2.Q5	It was hard to extract the peg from the hole.
E2.Q6	It was physically tiresome to accomplish the task.
E2.Q7	It was psychologically tiresome to accomplish the task.

the user through the telemanipulation framework is $Z_t = f_e/v_h = f_e/v_m = f_e/v_s = f_e/v_e = Z_e$, that is, i.e., the remote environment impedance, proving the transparency of the two frameworks in absence of delay. In the case of TIFT^2 (right column) a little different between z_m and z_s can be noticed. This is due to the low stiffness used by the user (see K_z in the third row), that combined with the non perfect dynamic compensation causes a little drift between master and slave position. For the same reason, also a slight difference in the force sensed and fed back to the user is present.

Moreover, the advantages of the inclusion of the Z_{C_s} branch in $N_{s,ext}$ are visible looking at the energy flows at the slave side (last rows of the plots of Fig. 11). The compensator K_s included in $N_{s,ext}$ stores certain amount of energy in the network and, consequently, damps the energy flux $E^{R,Out}_{N_s}$ that results always smaller than $E^{L,In}_{N_s}$, even in absence of delay (see the FT^2 and TIFT^2 cases of Fig. 11(a)). This damping factor is always persistent and has the consequence to strengthen the structure with respect to the passivity condition of (23), as also explained in Fig. 4.

7.1 Experiment 1 discussion

The advantages of the proposed two-channel architecture is immediately visible in the results relative to this experiment. All the plots of Fig. 11 clearly show that in the FT^2 and TIFT^2 cases no force is fed back to the user until a real contact occurs (green bands). This is a confirmation that, tuning the controllers as explained in Sec. 3, the phantom force phenomenon is avoided. This is also reflected in the fatigue index (Fig. 12(b)). Indeed, while in the no delay case the normalized $\overline{E}_{arm}$ of FT^2 and TIFT^2 are close to the 4C's, they decrease with respect to the latter proportionally to the rise of the delay. The statistical significance of normalized $\overline{E}_{arm}$ results is confirmed by the p-values reported in the last two lines of Table 3, always lower than 0.05 in the delayed scenarios. The absence of phantom forces is also appreciated by the user, as shown by the results of the questionnaire of Tab. 2 depicted in Fig. 13. Of particular interest for this aspect are the statements E1.Q1, E1.Q2, E1.Q3 and E1.Q5. In the 0 delay case, these statements scored the same for all the three control architectures (low for the all of them). Referring to the 4C architecture, when we move to the higher delay the score of E1.Q1 drastically increases (indicating a major effort to move the interface), and the same happen for the others, indicating an higher difficulty to recognize the contact (E1.Q2), to move away from it (E1.Q3, closely
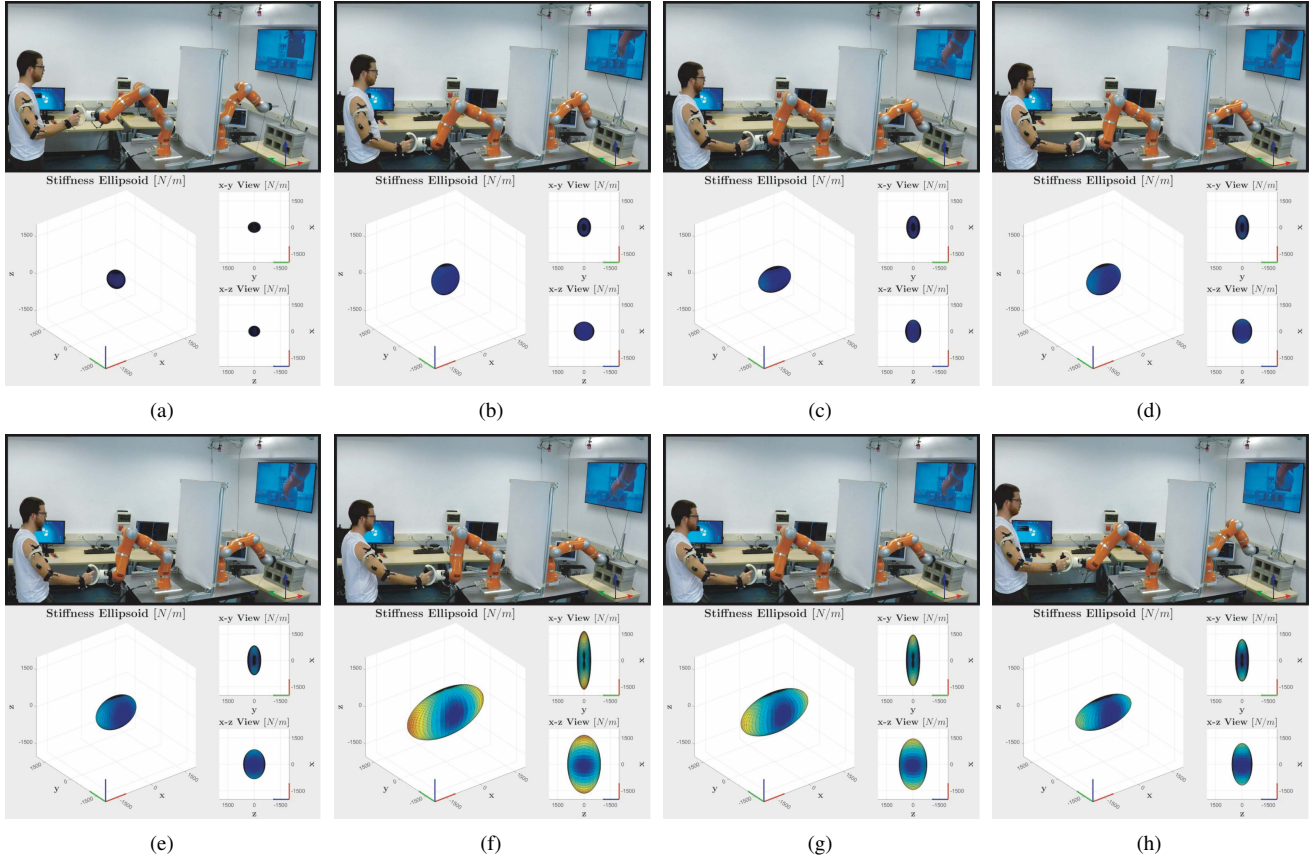
Figure 14. Frame sequence of the peg in hole task with $T_{rs} = 500ms$ executed with the proposed TIFT^2 architecture extrapolated from Extension 1: starting from an initial position (a), the user explores the remote environment and get closer to the hole (b). When close enough, he start the approaching phase, in which he tries to align the peg with the hole, using the help of the force feedback (c)-(d). Once the peg is aligned, the user starts starts inserting the peg (frames (e)-(f)) and when the insertion is completed he pulls the peg out (frames (g)-(h)). The images show two points of view (general view, top-left corner, and interaction view, top-right corner), together with the stiffness ellipsoid (bottom-left corner, resulting from (40)) and the interaction forces between the slave and the environment (bottom-right corner). From the images it is possible to observe the change of the stiffness ellipsoid both in volume and axis, depending on the phase of the task: i.e., while in the exploring and approaching phase (frames (c)-(d)) the ellipsoid is small and almost spherical, its shape changes both in volume and principal axis during the insertion and extraction phases (frames (c)-(d)), showing a rigid behavior along the hole direction and a more compliant behavior along the other axis.

related to E1.Q1) and a higher physical fatigue (E1.Q5), all results that indicates a less usability of the setup. At the same time, these statements maintained almost the same scores for both the FT^2 and TIFT^2, suggesting that for these solutions the setup usability and user's experience are less influenced by the delay than the 4C architecture.

The advantages of variable stiffness used through tele-impedance during the experiments can be seen in all the cases of Fig. 11, observing the contact force f_e^z of the second row. During the task, lower the interaction forces demonstrate a better performance, regardless the delay in the communication. All the experiments with TIFT^2 present lower interaction forces than 4C and FT^2, difference that increase together with the delay. This is confirmed also in the bar plots of Fig. 12(a), in which we see that even if all the $\overline{f}_{e,max}^z$ increased with the delay, the ones of TIFT^2 are always lower than the other two, that on the contrary are always higher and similar to each other. The reason is, again, the low stiffness profiles imposed by the user arm stiffness. While in 4C and FT^2 the control stiffness is constant and high (400 N/m), in TIFT^2 it copies the one of the user that, during exploration, adopt a low stiffness profiles. Indeed,

the users maintain a stiffness along z between 100 and 200 N/m c.a. When a delay in the communication occurs, a low stiffness allows to gently interact with the environment waiting for the user's perception and reaction, something that high stiffnesses don't allow. Also for $\overline{f}_{e,max}^z$, the statistical significance of these results is confirmed by the relative p-values always lower than 0.05 in the delayed scenarios, as reported in the first two lines of Table 3.

7.2 Experiment 2 discussion

Fig. 15 shows an example of peg-in-hole task executed with TIFT^2 with $T_{rt} = 500$ ms. The hole axis is parallel to x. As depicted, the task can be divided in three phases: the 'exploration phase'(green band), the 'approach phase'(yellow band) and the 'insertion/extraction phase'(red band). During the exploration, the user moves quite fast, using a low stiffness profile. When close to the hole, the approach phase begins, in which the velocity decreases and a fine adjustment of the position is done. In this second phase a medium-low stiffness profile is maintained and allows to decrease the undesired contact forces, similar to the Experiment 1. As soon as the peg is aligned with the
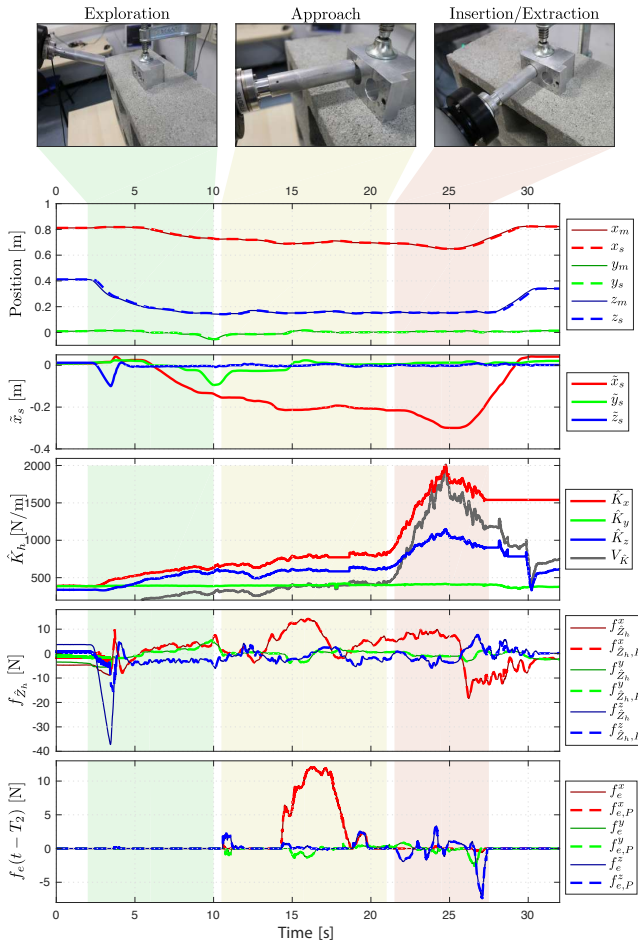
Figure 15. Peg-in-hole task with TIFT^2 and $T_1 = T_2 = 250$ ms. The hole axis is parallel to x. First row: master and slave linear positions. Second row: slave linear position errors. Third row: human linear stiffness profiles and ellipsoid volume ($V_{\hat{K}}$). Fourth row: slave commanded and passivated linear forces. Fifth row: environment force commanded to the master and passivated ones.

hole, the user naturally increases the stiffness mostly along the x direction, through the CMS-CDS technique explained in Subsec. 5.1, to start the insertion phase. This stiffness strategy is beneficial in the peg-in-hole. Indeed, the rigidity along the hole axis allows to exert a large force along that direction, forcing the peg to enter the hole. At the same time, a more compliant behavior along the remaining axes enables the slave to self-adapt its position and compensate for possible misalignment along those directions, despite any delay profiles. This stiffness profile is maintained during the whole insertion/extraction phase. Once the peg is extracted, the user relaxes and the stiffness is reduced as a consequence. This same behavior can be observed in Extension 1, where the on-line stiffness regulation of the tele-impedance CMS-CDS control is highlighted. It is also possible to observe the stable behavior of the system, despite the high communication delay profile.

This kind of behavior and interaction of the system would not be possible in both 4C and FT^2, since no on-line stiffness modulation is foreseen. With a delayed communication, the absence of tele-impedance control increases the environment interaction forces. It complicates the inserting/extracting phase as well: if a fixed high stiffness is chosen, the
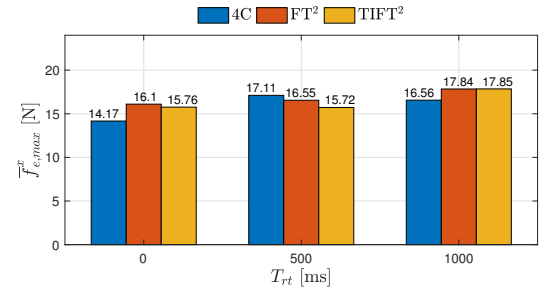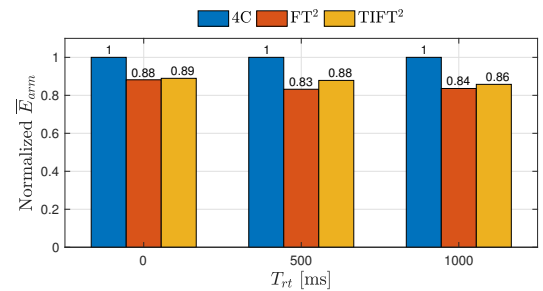

(a) Average maximum force $\overline{f}^x_{e,max}$ during the insertion/extraction phase of peg-in-hole task.
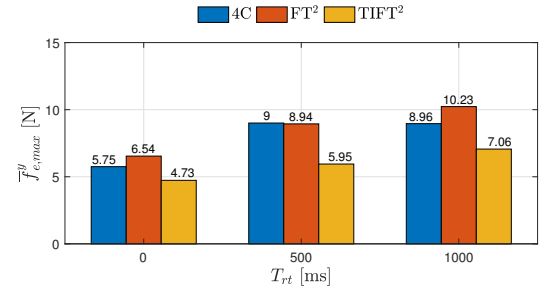
(b) Average maximum force $\overline{f}^y_{e,max}$ during the insertion/extraction phase of peg-in-hole task.
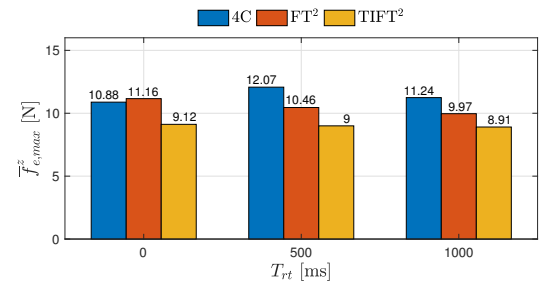
(c) Average maximum force $\overline{f}^z_{e,max}$ during the insertion/extraction phase of peg-in-hole task.

(d) Average EMGs $\overline{E}_{arm}$ normalized w.r.t. 4C case: the lower the better.

Figure 16. Performances comparison between 4C, FT^2 and TIFT^2 during the peg-in-hole experiment. Averages values of (a) maximum force along x, (b) maximum force along y, (c) maximum force along z and (d) average EMGs normalized w.r.t. 4C case. Lower values correspond to better performances.

compensation for misalignment is harder, while the insertion becomes more difficult with low stiffnesses, due to the low clearance between the peg and the hole. This is what the results of this experiments illustrate, as depicted in the second and third plots of Fig. 16. Indeed, TIFT^2 records the lower values for the maximum forces along y (Fig. 16(b)) and z (Fig. 16(c)) for all the delays. The same can not be said for the maximum force along x, really similar

Table 5. *p*-values resulting from Krustal-Wallis test of $\overline{f}^x_{e,max}$, $\overline{f}^y_{e,max}$, $\overline{f}^z_{e,max}$ and normalized $\overline{E}_{arm}$ data relative to Experiment 2. Green cells correspond to *p*-values lower than $\alpha = 0.05$, red cells to higher *p*-values.

		T_{rt}		
		0 ms	500 ms	1000 ms
$\overline{f}^x_{e,max}$	4C vs. FT^2	0.4420	0.6048	0.9764
	4C vs. TIFT^2	0.5742	0.3077	0.8708
	FT^2 vs. TIFT^2	0.8476	0.5844	1
$\overline{f}^y_{e,max}$	4C vs. FT^2	0.6574	0.6361	0.5946
	4C vs. TIFT^2	0.2805	0.0036	0.0459
	FT^2 vs. TIFT^2	0.0713	0.0358	0.0333
$\overline{f}^z_{e,max}$	4C vs. FT^2	0.9176	0.3593	0.7788
	4C vs. TIFT^2	0.0837	0.0045	0.0104
	FT^2 vs. TIFT^2	0.1242	0.1206	0.0314
norm. $\overline{E}_{arm}$	4C vs. FT^2	0.2028	0.2028	0.1062
	4C vs. TIFT^2	0.0338	0.0338	0.0154
	FT^2 vs. TIFT^2	0.8946	0.8253	0.7055

(a) $T_{rt} = 0$ ms.

(b) $T_{rt} = 500$ ms.
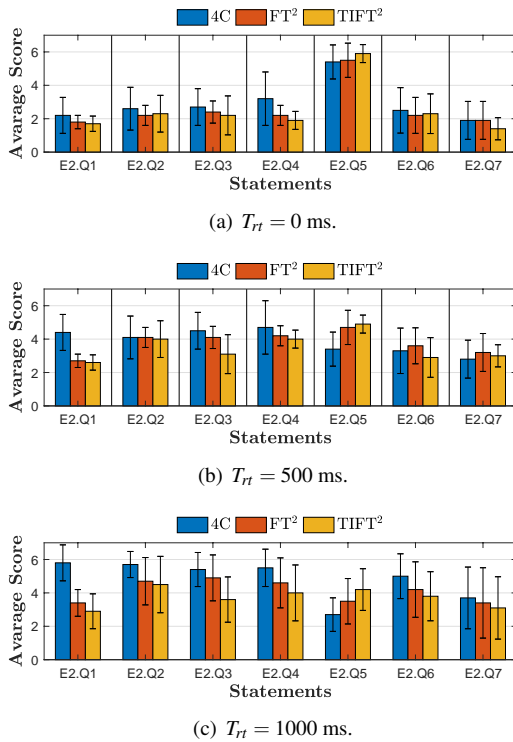
(c) $T_{rt} = 1000$ ms.

Figure 17. Average scores of the statements of Experiment 2 questionnaire (Tab. 2) in (a) $T_{rt} = 0$ ms, (b) $T_{rt} = 500$ ms and (c) $T_{rt} = 1000$ ms cases.

to the others, (Fig. 16(a)) but, as explained above, this is because the force along that axis directly depends on the will of the user, differently from the other two. Regarding the fatigue, the results depicted in Fig. 16(d) show again that 4C demonstrate a higher effort of the user than FT^2 and TIFT^2, even if not so clean-cut as in the first experiment results. This may be due to the complexity of the task,

that generally requires a higher effort and concentration. This whole analysis is also supported by the results of the Kruskal-Wallis tests, reported in Table 5, and confirmed by the result of the questionnaire of Tab. 4 depicted in Fig. 17. E2.Q1 results confirm that the phantom force effect complicate the interface handling. E2.Q2 scores show that the increment of delay worsen the peg insertion with all the architectures, while from E2.Q3 seems that TIFT^2 gives the best sensation in terms of peg insertion for any delay. E2.Q4 results strengthen our hypothesis asserting that TIFT^2 simplifies the insertion management. On the contrary, the result of E2.Q5 suggests that TIFT^2 complicates the peg extraction. This result could be caused by a lower impedance used by the subjects, compared with the other two architectures. Being more compliant, the interaction forces are naturally lower. Nonethess, with the increment of the communication delay also the possibility of momentary misalignment between the master and the slave position increment. In tasks like the peg-in-hole, this misalignment can be particularly annoying, especially to non-experienced and non-trained users, as it can be the cause of higher friction forces (not defeated due to the low impedance).

7.3 General discussion

A general picture about the performance of the introduced FT^2 and TIFT^2 architectures can be drawn considering the results of the two experiments. In can be divided into three aspects: *interaction force*, *user effort* and *user preference*.

Interaction forces: Bar plots of Fig. 12(a) and Fig. 16 show that almost same interaction forces are achieved with 4C and FT^2, while TIFT^2 exhibits alway lower forces and then higher performance (apart from the null delay cases). An exception is registered for $\overline{f}^x_{e,max}$ in the Peg-in-Hole experiment, for the reasons already discussed in Subsec. 7.2. These observations are also confirmed by the Krustal-Wallis test results of Tab. 3 and Tab. 5. Indeed, for both experiments, the test conducted on the interaction forces shows no statistical significance between 4C and FT^2, while the data of TIFT^2 assume statistical difference with respect to the other only when the communication delay is not null. The similarity of the interaction force profiles between 4C and FT^2 is something that was expected, considering that the force commanded at the slave end-effector is the same (from the equivalence of $F_{C_s,tot}$ in 4C (13) and FT^2 (22), and the fact that the slave impedance controller is tuned the same for both architectures). In the same way, also a better performance of TIFT^2 was expected, as the slave controller gains follow the user estimated ones that, normally, operate with low stiffness, unless a power task is demanded (see Fig. 11 and Fig. 15). Naturally, if a lower value is chosen for the fixed stiffness used in 4C and FT^2, the two architectures would perform closer or even better than the TIFT^2. As explained in Subsec. 6.1, the stiffness used in 4C and FT^2 has been tuned to be in the middle of the range of human stiffness and large enough to compensate for modeling uncertainties and friction. This second aspect is really important: if on one side low gains mean lower interaction forces, on the other the position tracking could could be relevant and even debilitating during precise movements. 4C and FT^2 do not embed the tele-impedance paradigm, meaning that

the user cannot correct the tracking error and regulate the slave precision by simply adjusting its own impedance. Instead, s/he would need to compensate directly correcting its position, eventually moving from the real desired position with possibly effects also on the feedback perception.

User effort: Bar plots of Fig. 12(b) and Fig. 16(d) show that the user fatigue in accomplishing the two experimental tasks with FT^2 and $TIFT^2$ is the same, in both cases lower than with 4C architecture. These results are also confirmed by the results of Krustal-Wallis tests, in particular the ones of Experiment 1. Indeed, results of Tab. 3 show that no statistical difference is detected between FT^2 and $TIFT^2$, while it is measured in 4C vs. FT^2 and 4C vs. $TIFT^2$ in non-null delay scenarios. Krustal-Wallis test results of Experiment 2 (Tab. 5) are less neat, probably due to the high complexity of the experiment itself.

The lower effort demanded by the new architectures is an expected result, and it has to be attributed to the cancellation of the phantom force. Indeed, the phantom force is displayed as soon as any small delay in the communication is present. Being opposite to the movement direction, this force demand a greater effort and drain energy to the user. Its effect could be mitigated choosing lower gains for Z_{C_m} (13), but it can not be completely canceled (or better it can be nullifying the gains of Z_{C_m}, that is equivalent to adopt the three-channel scheme corresponding to (16) and Fig. 2(b)).

User preference: The analysis of the results of the questionnaires reported in Tab 2 and 4 have been extensively discussed in the previous subsections. Apart from E2.Q5, all these results show that the subjects experience a better control of the interaction using the new $TIFT^2$ architecture, that are synonym of an increased usability of the setup. All these results support the qualitative evaluation provided in Table 1 of the introduction section. Together, they confirm the goal of this paper to provide a framework that subsumes the quality of both fully transparent teleoperation frameworks and robust and reliable tele-impedance control in the ultimate effort to provide the user with a better performing and usable setup.

7.4 Practical showcase

As an additional example of practical dynamic task that can be executed with the proposed $TIFT^2$ architecture, Extension 2 shows the sanding of car frame portion with two different communication profiles ($T_{rt} = 100, 200$ ms). Fig. 18 shows four frames extrapolated from the Extension 2 that summarize the various phases of this task.

For this task, the robots end-effector are modified: a Pisa/IIT SoftHand is used as slave hand effector, while an handle with an embedded trigger is mounted on the master robot, and is used to command the closure of the Pisa/IIT SoftHand. The master handle is mounted on a custom safety magnetic clutch. This clutch is inspired by the one developed for the DLR's bi-manual haptic device (Hulin et al. 2011) and is directly linked to the KUKA emergency button pins. The use of Pisa/IIT SoftHand driven by the trigger enables the possibility to easily grasp and use objects/tools at the slave side. The peculiarities of the Pisa/IIT SoftHand (i.e. its capacity to self adapt the grasp to the grasped object and its high robustness and resilience) allow the user to not dedicate

too much attention the grasping and instead focus on the accomplishment of the task. Details on the hand, the trigger and their interconnection can be found in (Della Santina et al. 2017).

Also in this example, the stability and the ease of use of the system despite the communication delay are clearly appreciable.

8 Conclusions

This paper presented a two-channel architecture (the FT^2) for bilateral teleoperation that respects full transparency requirements together with a pool of complex and dynamic multi-subject experiments and an extensive evaluation of the results. The proposed solution halves the signals needed by classic architecture in a way to uncouple as much as possible the master and slave sides and to avoid the so-called 'phantom forces' during free-environment motion. In its building process, it has also been shown that the transmitted impedance with communication delays is closer to the ideal delayed impedance for our proposed architecture than for others at the state of the art. These factors led to an increment of comfort and correctness of perception of the remote environment, as well as a substantial reduction of the user fatigue. The proposed architecture allowed also to strengthen the network with respect to passivity condition while using the Time Domain Passivity Approach to assure the stability over delays. Regarding the removal of the phantom force, a potential drawback for novice users has to be underlined: the absence of a phantom force has been demonstrated to be convenient in terms of user effort and perception. Nevertheless, in case of high communication delays, an unexpected contact in the remote environment fed back to the master side could find the operator unprepared. In cases of certain power tasks, if the user reaction is not prompt and appropriate, the consequence can be the damage of the system and also of the operator itself.

Furthermore, the authors proposed the inclusion of the tele-impedance paradigm, and called the architecture including it $TIFT^2$, to overcome the loss of transparency, allowing the slave to follow not only the user's position and forces but also its stiffness profiles. It has been shown that tele-impedance allows to decrease substantially the interaction forces during an environment exploration phase, and to increase them together with the robot accuracy when precision tasks are demanded while maintaining the same level of remote perception and telepresence. The only practical disadvantage of the inclusion of tele-impedance is the loss of a *plug-and-play* system, as TI requires an initial user-dependent calibration.

These results have been confirmed also at the user subjective side. Indeed, from the questionnaire statement scores we have inferred that, introducing a delay in the communication, the classic solution lacks in the interface handling and remote perception and interaction. On the contrary, even if inevitably deteriorated by the delays, the user's judgment on the new architecture didn't change to much across the different delayed conditions.

From both objective and subjective side, it can be inferred that the new proposed architectures, the FT^2 and $TIFT^2$, decrease the user fatigue compared to the classic 4C scheme.

| (a) | (b) | (c) | (d) |
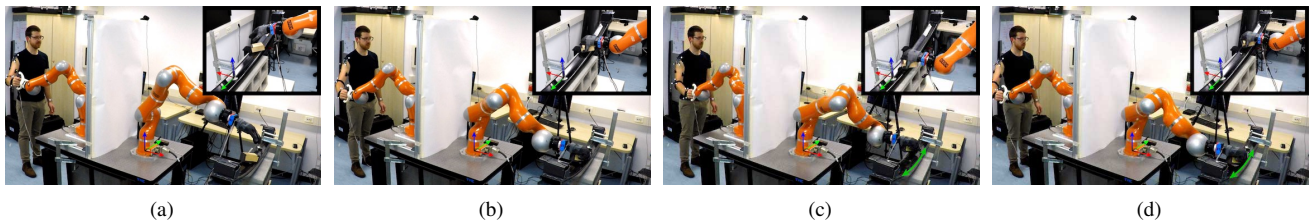
Figure 18. Frame sequence of the car frame sanding with a consistent communication delay, extrapolated from Extension 2: starting from an initial position (a), the user approaches and grabs a wooden block covered with sandpaper (b), and starts the sanding through an oscillatory movement, as highlighted with the arrowed line in frames (c)-(d). The images report two points of view: one showing the whole setup and one showing only the car frame (upper-right corner).

.

Furthermore, compared with 4C and FT^2, the inclusion of the tele-impedance paradigm in TIFT^2 helps in decreasing the interaction forces when a delay in the communication is present and a compliant interaction is desired.

All these results confirm the achievement of the target of this paper: find an improved architecture for bilateral teleoperation that, without renouncing to high transparency performances, facilitates its use, reduces the user's fatigue, and enhances his/her experience.

Acknowledgements

Appendix A: Index to multimedia Extensions

Extension	Media Type	Description
1	Video	Peg in hole experiment with 500ms round-trip communication delay
2	Video	Practical task example: Sanding with different communication delay profiles

References

Ajoudani A (2016) *Transferring human impedance regulation skills to robots*, volume 110. Springer.

Ajoudani A, Fang C, Tsagarakis N and Bicchi A (2017) Reduced-complexity representation of the human arm active end-point stiffness for supervisory control of remote manipulation. *The International Journal of Robotics Research* : 0278364917744035.

Ajoudani A, Gabiccini M, Tsagarakis N, Albu-Schäffer A and Bicchi A (2012) Teleimpedance: Exploring the role of common-mode and configuration-dependant stiffness. In: *Proceedings of 12th IEEE-RAS International Conference on Humanoid Robots (Humanoids), 2012*. pp. 363–369.

Albu-Schäffer A, Ott C, Frese U and Hirzinger G (2003) Cartesian impedance control of redundant robots: Recent results with the dlr-light-weight-arms. In: *2003 IEEE International Conference on Robotics and Automation (Cat. No. 03CH37422)*, volume 3. IEEE, pp. 3704–3709.

Alfi A and Farrokhi M (2008) A simple structure for bilateral transparent teleoperation systems with time delay. *Journal of Dynamic Systems, Measurement, and Control* 130(4): 044502.

Aliaga I, Rubio A and Sanchez E (2004) Experimental quantitative comparison of different control architectures for master-slave teleoperation. *IEEE transactions on control systems technology* 12(1): 2–11.

Anderson RJ and Spong MW (1989) Bilateral control of teleoperators with time delay. *IEEE Transactions on Automatic control* 34(5): 494–501.

Artigas J (2014) *Time domain passivity control for delayed teleoperation*. PhD Thesis, PhD thesis, Universidad Politécnica de Madrid.

Artigas J, Balachandran R, Riecke C, Stelzer M, Weber B, Ryu JH and Albu-Schaeffer A (2016) Kontur-2: force-feedback teleoperation from the international space station. In: *Proceedings of IEEE International Conference on Robotics and Automation (ICRA), 2016*. pp. 1166–1173.

Artigas J, Ryu JH and Preusche C (2010) Time domain passivity control for position-position teleoperation architectures. *Presence* 19(5): 482–497.

Balachandran R, Jorda M, Artigas J, Ryu JH and Khatib O (2017) Passivity-based stability in explicit force control of robots. In: *Proceedings of IEEE International Conference on Robotics and Automation (ICRA), 2017*. IEEE, pp. 386–393.

Chawda V, Van Quang H, O'Malley MK and Ryu JH (2014) Compensating position drift in time domain passivity approach based teleoperation. In: *Proceedings of IEEE Haptics Symposium (HAPTICS), 2014*. pp. 195–202.

Della Santina C, Piazza C, Gasparri GM, Bonilla M, Catalano MG, Grioli G, Garabini M and Bicchi A (2017) The quest for natural machine motion: An open platform to fast-prototyping articulated soft robots. *IEEE Robotics & Automation Magazine* 24(1): 48–56.

Desbats P, Geffard F, Piolain G and Coudray A (2006) Force-feedback teleoperation of an industrial robot in a nuclear spent fuel reprocessing plant. *Industrial Robot: An International Journal* 33(3): 178–186.

Fang C, Ajoudani A, Bicchi A and Tsagarakis NG (2018) A real-time identification and tracking method for the musculoskeletal model of human arm. In: *Proceedings of IEEE International Conference on Systems, Man, and Cybernetics (SMC), 2018*. pp. 3472–3479.

Ferraguti F, Preda N, Manurung A, Bonfe M, Lambercy O, Gassert R, Muradore R, Fiorini P and Secchi C (2015) An energy tank-based interactive control architecture for autonomous and

teleoperated robotic surgery. *IEEE Transactions on Robotics* 31(5): 1073–1088.

Franken M, Stramigioli S, Misra S, Secchi C and Macchelli A (2011) Bilateral telemanipulation with time delays: A two-layer approach combining passivity and transparency. *IEEE transactions on robotics* 27(4): 741–756.

Guizzo E and Ackerman E (2015) The hard lessons of darpa's robotics challenge [news]. *IEEE Spectrum* 52(8): 11–13.

Hannaford B (1989) A design framework for teleoperators with kinesthetic feedback. *IEEE transactions on Robotics and Automation* 5(4): 426–434.

Hannaford B and Ryu JH (2002) Time-domain passivity control of haptic interfaces. *IEEE Transactions on Robotics and Automation* 18(1): 1–10.

Hashtrudi-Zaad K (2000) *Design, implementation and evaluation of stable bilateral teleoperation control architectures for enhanced telepresence*. PhD Thesis, University of British Columbia.

Hashtrudi-Zaad K and Salcudean SE (2001) Analysis of control architectures for teleoperation systems with impedance/admittance master and slave manipulators. *The International Journal of Robotics Research* 20(6): 419–445.

Hashtrudi-Zaad K and Salcudean SE (2002) Transparency in time-delayed systems and the effect of local force feedback for transparent teleoperation. *IEEE Transactions on Robotics and Automation* 18(1): 108–114.

Held RM and Durlach NI (1992) Telepresence. *Presence: Teleoperators & Virtual Environments* 1(1): 109–112.

Hirche S, Bauer A and Buss M (2005) Transparency of haptic telepresence systems with constant time delay. In: *Proceedings of 2005 IEEE Conference on Control Applications, 2005. CCA 2005*. IEEE, pp. 328–333.

Hokayem PF and Spong MW (2006) Bilateral teleoperation: An historical survey. *Automatica* 42(12): 2035–2057.

Hulin T, Hertkorn K, Kremer P, Schätzle S, Artigas J, Sagardia M, Zacharias F and Preusche C (2011) The dlr bimanual haptic device with optimized workspace. In: *Proceedings of IEEE International Conference on Robotics and Automation (ICRA), 2011*. pp. 3441–3442.

Iida W and Ohnishi K (2004) Reproducibility and operationality in bilateral teleoperation. In: *Proceedings of 8th IEEE International Workshop on Advanced Motion Control, 2004*. pp. 217–222.

Imaida T, Yokokohji Y, Doi T, Oda M and Yoshikawa T (2004) Ground-space bilateral teleoperation of ets-vii robot arm by direct bilateral coupling under 7-s time delay condition. *IEEE Transactions on Robotics and Automation* 20(3): 499–511.

Khatib O, Yeh X, Brantner G, Soe B, Kim B, Ganguly S, Stuart H, Wang S, Cutkosky M, Edsinger A, Mullins P, Barham M, Voolstra CR, Salama KN, L'Hour M and Creuze V (2016) Ocean one: A robotic avatar for oceanic discovery. *IEEE Robotics Automation Magazine* 23(4): 20–29. DOI:10.1109/MRA.2016.2613281.

Laghi M, Ajoudani A, Catalano M and Bicchi A (2017) Tele-impedance with force feedback under communication time delay. In: *Proceedings of IEEE/RSJ International Conference on Intelligent Robots and Systems (IROS), 2017*. pp. 2564–2571.

Lawrence DA (1993) Stability and transparency in bilateral teleoperation. *IEEE transactions on robotics and automation* 9(5): 624–637.

Meli L, Pacchierotti C and Prattichizzo D (2017) Experimental evaluation of magnified haptic feedback for robot-assisted needle insertion and palpation. *The International Journal of Medical Robotics and Computer Assisted Surgery* 13(4).

Mitra P and Niemeyer G (2008) Model-mediated telemanipulation. *The International Journal of Robotics Research* 27(2): 253–262.

Natori K, Tsuji T, Ohnishi K, Hace A and Jezernik K (2010) Time-delay compensation by communication disturbance observer for bilateral teleoperation under time-varying delay. *IEEE Transactions on Industrial Electronics* 57(3): 1050–1062.

Negrello F, Settimi A, Caporale D, Lentini G, MPoggiani, Kanoulas D, Muratore L, Luberto E, Santaera G, Ciarleglio L, Ermini L, Pallottino L, Caldwell D, Tsagarakis N, Bicchi A, Garabini M and Catalano M (2018) Walk-man humanoid robot: Field experiments in a post-earthquake scenario. *Robotics and Automation Magazine (RAM), IN PRESS* .

Niemeyer G, Preusche C and Hirzinger G (2008) Telerobotics. In: *Springer Handbook of Robotics*. Springer, pp. 741–757.

Niemeyer G and Slotine JJ (1997) Using wave variables for system analysis and robot control. In: *Proceedings of IEEE International Conference on Robotics and Automation, 1997*, volume 2. pp. 1619–1625.

Pacchierotti C, Tirmizi A, Bianchini G and Prattichizzo D (2015) Enhancing the performance of passive teleoperation systems via cutaneous feedback. *IEEE Transactions on Haptics* 8(4): 397–409.

Panzirsch M, Artigas J, Ryu JH and Ferre M (2013) Multilateral control for delayed teleoperation. In: *2013 16th International Conference on Advanced Robotics (ICAR)*. IEEE, pp. 1–6.

Panzirsch M, Ryu JH and Ferre M (2019) Reducing the conservatism of the time domain passivity approach through consideration of energy reflection in delayed coupled network systems. *Mechatronics* 58: 58–69.

Pratt G and Manzo J (2013) The darpa robotics challenge [competitions]. *IEEE Robotics & Automation Magazine* 20(2): 10–12.

Raju GJ, Verghese GC and Sheridan TB (1989) Design issues in 2-port network models of bilateral remote manipulation. In: *Proceedings, 1989 International Conference on Robotics and Automation*. IEEE, pp. 1316–1321.

Rebelo J and Schiele A (2015) Time domain passivity controller for 4-channel time-delay bilateral teleoperation. *IEEE transactions on haptics* 8(1): 79–89.

Ryu JH and Preusche C (2007) Stable bilateral control of teleoperators under time-varying communication delay: Time domain passivity approach. In: *Proceedings 2007 IEEE International Conference on Robotics and Automation*. IEEE, pp. 3508–3513.

Salcudean SE, Zhu M, Zhu WH and Hashtrudi-Zaad K (2000) Transparent bilateral teleoperation under position and rate control. *The International Journal of Robotics Research* 19(12): 1185–1202.

Schwarz M, Rodehutskors T, Droeschel D, Beul M, Schreiber M, Araslanov N, Ivanov I, Lenz C, Razlaw J, Schüller S, Schwarz D, Topalidou-Kyniazopoulou A and Behnke S (2017) Nimbro rescue: Solving disaster-response tasks with the mobile manipulation robot momaro. *Journal of Field Robotics* 34(2): 400–425.

Shukla A and Karki H (2016) Application of robotics in onshore oil and gas industry—a review part i. *Robotics and Autonomous Systems* 75: 490–507.

Smith OJ (1959) A controller to overcome dead time. *iSA journal* 6(2): 28–33.

Suzuki A and Ohnishi K (2013) Frequency-domain damping design for time-delayed bilateral teleoperation system based on modal space analysis. *IEEE Transactions on Industrial Electronics* 60(1): 177–190.

Wright J, Trebi-Ollennu A, Hartman F, Cooper B, Maxwell S, Yen J and Morrison J (2005) Driving a rover on mars using the rover sequencing and visualization program. In: *International Conference on Instrumentation, Control and Information Technology (Okayama University, Okayama 2005)*.

Xu X, Cizmeci B, Al-Nuaimi A and Steinbach E (2014) Point cloud-based model-mediated teleoperation with dynamic and perception-based model updating. *IEEE Transactions on Instrumentation and Measurement* 63(11): 2558–2569.

Xu X, Cizmeci B, Schuwerk C and Steinbach E (2016) Model-mediated teleoperation: toward stable and transparent teleoperation systems. *IEEE Access* 4: 425–449.